This is the accepted manuscript made available via CHORUS. The article has been published as:

Experimental search for toroidal high-spin isomers in collisions of math xmlns="http://www.w3.org/1998/Math/MathML">mrow>mmultiscripts>mi>Si/mi>mprescripts>/mprescripts>none>/none>mn>28/mn>/mmultiscripts>mo>+/mo>mmultiscripts>mi mathvariant="normal">C/mi>mprescripts>/mprescripts>none>/none>mn>12/mn>/mmultiscripts>/mrow>/math> at 35 MeV/nucleon with the Forward Array Using Silicon Technology

A. Hannaman, B. Harvey, A. B. McIntosh, K. Hagel, A. Abbott, A. Fentress, J. Gauthier, T. Hankins, Y.-W. Lui, L. McCann, L. A. McIntosh, S. Regener, R. Rider, S. Schultz, M. Q. Sorensen, J. Tobar, Z. N. Tobin, and S. J. Yennello

Phys. Rev. C **109**, 054615 — Published 16 May 2024

DOI: 10.1103/PhysRevC.109.054615

Experimental Search for Toroidal High-Spin Isomers in Collisions of ^{28}Si + ^{12}C at 35 MeV/nucleon with the Forward Array Using Silicon Technology (FAUST)

A. Hannaman[a,b,*], B. Harvey[a,c], A.B. McIntosh[a], K. Hagel[a], A. Abbott[a,b], A. Fentress[a,b], J. Gauthier[a], T. Hankins[a,b], Y.-W. Lui[a], L. McCann[a,b], L.A. McIntosh[a], S. Regener[a], R. Rider[a,b], S. Schultz[a,b], M.Q. Sorensen[a,b], J. Tobar[a,b], Z.N. Tobin[a,b], S.J. Yennello[a,b]

[a] *Cyclotron Institute, Texas A&M University, College Station, TX 77843, USA*
[b] *Chemistry Department, Texas A&M University, College Station, TX 77843, USA*
[c] *Physics Department, Texas A&M University, College Station, TX 77843, USA*

Abstract

Ground state stable nuclei typically have near-spherical geometries but may exhibit exotic shapes and form α-particle clusters within their bulk if given excitation energy and/or angular momentum. It is predicted that such clustering can promote the production of angular-momentum stabilized toroidal nuclei. Previous experiment and theory suggest that such states may be evidenced by narrow resonances at high excitation energy in peripheral intermediate energy heavy-ion collisions. There has been recent focus on potential evidence for toroidal states in the α-particle disassembly of ^{28}Si in collisions of ^{28}Si + ^{12}C at 35 MeV/nucleon; however, prior evidence is limited by the angular resolution and statistical uncertainties that exist in the measurement. The present work aims to measure the excitation energy distribution for these disassembly events with improved angular resolution and reduced statistical uncertainty using the Forward Array Using Silicon Technology (FAUST). FAUST is equipped with resistive dual-axis duo-lateral (DADL) position-sensitive silicon detectors capable of sub-millimeter position resolution. The performance and response of the array was previously characterized in detail to accurately predict the expected resolution of measuring narrow resonances. The measured excitation energy distributions for 7- and 8-α disassembly events showed no strong evidence for highly excited states at the cross section and widths suggested by previous experiment. Further investigation of collision properties that lead to these exit channels revealed challenges in isolating clean projectile-mass decays, where many 7-α events do not originate from a single ^{28}Si source. A statistical likelihood analysis was performed to determine the sensitivity of the present measurement for confidently determining resonant yield, providing an upper limit to toroidal high-spin isomer cross section as a function of the excitation energy and width of potential states.

*Corresponding Authors
Email addresses: andyhannaman@tamu.edu (A. Hannaman), alanmcintosh@tamu.edu (A.B. McIntosh)

1. Introduction

The first evidence that suggested atomic nuclei may have geometries deviating from a spherical description emerged when the quadrupole moments of ^{151,153}Eu were more than an order of magnitude greater than that attainable by single nucleon motion, suggesting a collective deformation [1]. This evidence sparked the pioneering work by Bohr, Mottelson, Nilsson, Rainwater, and Wheeler to develop a nuclear model that accounted for the relationship between individual-particle and collective motion consistent with observed phenomena; Bohr, Mottelson, and Rainwater won the Nobel Prize for these efforts in 1975 [2, 3, 4, 5]. Nuclear deformation was required to resolve the existence of rotational bands despite collective rotation of a sphere about a symmetry axis being quantum mechanically forbidden. With the emergence of the shell model, Nilsson calculated how the single particle potentials changed as a function of quadrupole deformation, giving rise to new shell closures at certain deformation values [6]. While most observed phenomena could be explained by rather simple deformations (e.g., prolate, oblate), Wheeler considered the implications and feasibility of a toroidal deformation under certain conditions [7].

Wong, a student of Wheeler, expanded considerably on the idea, performing calculations to predict the stability conditions and structure properties for a range of nuclei using numerous models. In earlier work, Wong predicted toroidal states in the $40 \leq A \leq 70$ and $A \leq 250$ mass range where large shell effects in light nuclei and large Coulomb energies in heavier nuclei are advantageous for toroid stability [8, 9]. Large energy gaps were observed in the single particle potentials as a function of the toroidal deformation parameter R/d, where R is the major radius and d is the minor radius of the toroid. A modified liquid drop model including rigid body rotation was then used to predict what angular momentum would be necessary to form a stable toroid as a function of nuclear mass [10]. While the assumptions made in this calculation are rather stringent, it showed that the basic gross forces relevant to nuclear stability could support the existence of a toroidal nucleus over a large range in nuclear mass if given enough angular momentum. The stability of a nuclear toroid can be intuitively understood by comparison to a liquid toroid, where the rotational energy (and Coulomb energy) tends to expand the toroid and the attractive forces of the liquid (nuclear) bulk tend to contract the toroid. However, as nuclei are quantum mechanical systems, this collective rotation is forbidden. In reality, the total angular momentum of the toroid comes from the alignment of the individual nucleon angular momentum along the symmetry axis, inducing strong circulating currents [11, 12]. While the internal structure of this single-particle rotation is significantly different from collective rotation, their behavior is similar [13]. Wong has proposed two ways to populate such states experimentally: having a smaller projectile punch-through a larger target nucleus at small impact parameters, or populating the excitation energy and angular momentum of a toroidal state through deep inelastic heavy-ion collisions [12]. The former poses challenges when using charged-particle spectroscopy for such studies, as the low energy target-like toroidal breakup particles are difficult to measure and identify. Consequently, experimental efforts to produce and study toroidal nuclei primarily use the latter method.

In recent years, a number of powerful models have been used to further predict the prop-

erties and stability of toroidal nuclei. Staszczak and Wong used a cranked self-consistent Skyrme-Hartree-Fock calculation to generalize the possible existence of stable toroid configurations in the $28 \leq A \leq 52$ mass region for N=Z nuclei [14]. It was found that for a given quanta of angular momentum, the density configuration of a spherical nucleus would spontaneously take on a toroidal shape as the quadrupole moment constraint was decreased. These toroidal configurations emerge as local minima in the calculated excitation energy as a function of the quadrupole moment, with some quasi-stable states predicted for lighter nuclei (^{28}Si and ^{32}S) [14]. This study was even extended to non α-conjugate nuclei in the same mass range, showing similar predicted toroidal isomer properties as their α-conjugate counterparts [15].

Recently, experimental evidence for toroidal states in the 7-α breakup of ^{28}Si was reported, fueling interest in being able to predict and replicate the observed properties a priori [16]. Covariant density functional theory (CDFT) using the PC-PK1 and DD-ME2 density functionals replicated the previous prediction of the $44\hbar$ state in ^{28}Si, as well as finding additional states (local energy minima) for other values of angular momentum [17, 18]. It was also found that the predicted minor diameter of the torus is similar to the diameter of an α-particle. An α-localization function was used to confirm the minimum necessary conditions for α-clustering in the predicted high spin states [17]. The roughly linear correlation between the angular momentum and excitation energy is consistent with the picture of single-particle angular momentum alignment behaving similarly to collective rotation [19]. A separate phenomenological mean field calculation studied the validity of stabilized exotic deformations in the intermediate mass region, suggesting stability of toroidal geometries for both ^{28}Si and ^{32}S [20].

Using a different approach, Zheng and Bonasera developed and employed a semi-classical α-cluster model to predict experimental signatures of spin-induced toroidal α-breakup of ^{28}Si [21]. Unlike the static nature of CDFT, the time evolution of toroidal breakup and the effect of classical fluctuations was explored in this work. It is important to note that this work differed from previous calculations in that it did not inherently predict static toroid quasi-stability, instead averaging over many 7-α decay channel simulations to observe toroidal breakup geometries under set angular momentum conditions. These model calculations resulted in increased broadening of the excitation energy distributions with increasing angular momentum due to event averaging and classical fluctuations, suggesting that states can only be resolved in the lower spin (and lower excitation energy) regime where distributions do not significantly overlap.

While these predictions suggest that toroidal nuclear geometries are possible under the right conditions, it is important to consider which de-excitation pathways are probable. Experiments designed to search for toroidal nuclei using charged particle spectroscopy must be designed to efficiently and accurately measure such decay pathways. Given the success of the liquid drop model in reproducing many general properties of nuclear matter, it is natural to look at macroscopic fluid toroid behavior to gain insight to nuclear toroid behavior [22]. It is known that fluid toroids experience Plateau-Rayleigh instabilities that can cause symmetric breakup into smaller fragments of similar size [23, 24]. The number of breakup

fragments and finer details of the breakup mode time evolution depends on the rotational energy and aspect ratio [25]. However, properties unique to nuclear matter not accounted for in the macroscopic fluid analogue cannot be ignored; these include shell effects, Coulomb forces, clustering, decay fragment binding energies, and the discrete nature of nucleons. For example, Wong found that the liquid-drop type instabilities predicted for some toroidal nuclei are counteracted by large shell effects, giving toroidal shell closures [9]. Another study found that the theorized shell structure of hyperheavy (Z $\approx$ 130-180) nuclei may stabilize the toroidal configuration to breathing and sausage deformations [26]. Of course, further theoretical support is needed to better understand dominant breakup modes for lighter nuclei. Given the very high excitation energies ($\approx$150 - 200 MeV) of predicted states in the intermediate mass regime and the predicted aspect ratio and density providing an environment conducive to α-clustering, complete α-particle disassembly is a promising exit channel to search for such states. The existence of these high-spin toroidal isomers would be the first occurrence of a distinct nuclear resonant state this high in excitation energy as this region is well described as a continuum of states.

The first experimental evidence for toroidal high-spin isomers consistent with the work of Staszczak and Wong – and the primary motivation for this work – came from an experiment where collisions of ^{28}Si + ^{12}C at 35 MeV/nucleon were measured using the NIMROD detector array [27, 18, 14]. This experiment was not designed with the intent of searching for such states; however, when examining the excitation energy distribution for events with seven measured projectile-like α-particles, structure in the form of peaks was observed at very high excitation energy. To isolate the possible excited state contributions from the total spectrum, event mixing was used to produce an uncorrelated excitation energy distribution to serve as a background. After normalization of the background to the selected non-resonant portion of the experimental spectrum, a residual spectrum was produced by subtracting the experimental data from the normalized mixed event background. A semi-empirical model constrained by the general predicted spacing of neighboring angular momentum states was created to fit the data and extract properties of potential states. The extracted properties indicated that the three most statistically significant peaks may correspond to states with angular momentum of 28$\hbar$, 36$\hbar$, and 44$\hbar$. The width extracted from the fit ranged from 5-9 MeV (FWHM) for the highest yielding peaks, although the angular resolution of NIMROD suggests that states with infinitely narrow intrinsic widths (δ-resonances) at this excitation

E* (MeV)	Ang. Mom. ($\hbar$)	Stat. Sig. (σ)	Measured Width (FWHM)	σ (μb)
114	28	5.0	5.88 $\pm$ 2.36	—
126	36	7.9	8.57 $\pm$ 1.44	51 $\pm$ 13
138	44	7.1	8.03 $\pm$ 1.75	28 $\pm$ 7

Table 1: Experimentally determined properties of the potential toroidal high-spin isomer states observed in ref. [18]. Angular momentum is assigned by comparing to theory predictions. Statistical significance is determined by the yield above the normalized mixed event background. Cross section is estimated using AMD + GEMINI++ simulation data.

energy would give measured widths of similar magnitude. In the determination of the cross section for each state, all yield in the residual was assumed to originate from broad overlapping contributions from toroidal high-spin breakups. The cross section was estimated by interpolating the systematic calculations of Wilcke to obtain a total reaction cross section [28]. The total number of collisions measured (where at least one particle was detected) was scaled by the detection efficiency of NIMROD determined by using filtered AMD + GEMINI++ simulation data. A similar procedure was then performed to obtain the detection efficiency for the 7-α channel. This allowed for the yield within each peak in the residual spectrum to be scaled to a cross section, albeit with large systematic errors. A summary of the observed peak locations and extracted properties are shown in Table 1. Given the limitations of the NIMROD detector array for making such measurements, the authors suggested that an experiment with improved angular resolution is necessary to further identify and characterize these states.

The goal of this work is to perform a high angular resolution measurement with a significant increase in the number of measured 7-α events to reduce both the statistical and systematic uncertainties of previous measurement. If these states exist with the cross sections and widths reported in ref. [18], such a measurement could better determine their intrinsic widths, providing information about their lifetime and stability.

2. Experimental Details

2.1. Collision Systems

The primary reaction studied in this experiment was ^{28}Si at 35 MeV/nucleon impinged on a ^{12}C target in inverse kinematics. Additional reaction systems of ^{28}Si at 35 MeV/nucleon impinged on ^{28}Si,^{27}Al targets were also measured to explore the effect of target size and α-conjugation on potential toroidal state production. The experiment took place in June of 2021; all beams were accelerated using the K500 cyclotron at the Cyclotron Institute at Texas A&M University. Details of the measured collision systems are shown in Table 2.

Beam Species	Beam Energy (MeV/nucleon)	Target Material	Target Thickness (mg/cm^2)	Data Collection Duration	Events with Particle ID
^{28}Si	35	^{12}C	0.930	≈6 days	3.35×10^8
^{28}Si	35	^{27}Al	1.0	≈1 day	4.25×10^7
^{28}Si	35	^{28}Si	1.0	≈1 day	3.09×10^7

Table 2: Details for each collision system. The number of recorded collision events with identified charged particles are shown in the right column.

2.2. Forward Array Using Silicon Technology (FAUST)

The Forward Array Using Silicon Technology (FAUST) is designed to measure charged particle reaction products produced in intermediate energy heavy-ion collisions. The array consists of 68 Si/CsI(Tl) telescopes which provide nearly complete angular coverage from 2.3° to 34.5° with partial coverage down to 1.6° and up to 45.5°. The faces of the silicon detectors are resistive which allows the use of charge splitting for position measurement; for 25 MeV alpha particles produced in the present reactions the position resolution is 0.4 µm (≈0.2° angular resolution). Details and characterization of the DADL position and energy resolution attained in this experiment can be found in refs. [29, 30].

3. Quality Assessment of Data

Quantifying the general performance characteristics of FAUST is important for understanding all sources of measurement uncertainty. The average energy resolution (FWHM) for the 8.4 MeV α-decay peak from a radioactive ^{229}Th source is 1.3% for all DADL detectors, with some as good as 0.8%. For particles identified as α-particles using the ΔE-E technique, there exists a neutron double-hit background contamination of 1.2% and a ^{3}He contamination of 0.7% on average.

The quality in particle identification, energy calibration, and FAUST position calibration can be simultaneously assessed by determining the resolution of measured particle-unbound excited states. Given the energy and α-conjugation of the collision system, a significant amount of ^{8}Be is produced in the collisions. The ^{8}Be ground state is unbound and promptly decays into two α-particles with a relative energy of 92 keV [31]. The width in the α-α relative energy distribution associated with this decay that is measured in charged particle spectroscopy experiments is dominated by the energy and angular resolution of the detector apparatus due to the very narrow intrinsic width of the state (6 eV). The measured ^{8}Be ground state width is ≈45 keV FWHM in FAUST as shown in detail in ref. [30]. An even more sensitive probe of FAUST calibration accuracy is to inspect the measurement of known ^{12}C excited states that decay into 3 α-particles (e.g., the Hoyle state) [32]. The measured mean of the Hoyle state (7.67 MeV) is well within the literature value uncertainty (7.65 MeV±0.19), while the measured width (FWHM) is 0.104 MeV (9 eV intrinsic width) [33].

4. Results and Analysis

The formal analysis of the experimental data begins by discussing event kinematics and event selection requirements for preferentially selecting projectile-like α-disassembly events in Section 5. The main excitation energy analysis is presented in Section 6, including determination of the detection efficiency and resolution (Section 6.1), comparison to the prior measurement (Section 6.2), and discussion regarding the description of the background (Section 6.3). Partitioning of the experimental α-disassembly events into those more consistent with simultaneous or sequential decay is shown in Section 7. Momentum shape analysis is

used to further assess the characteristics of such decays in Section 8. A brief investigation into target mass and α-conjugation effects on toroidal state production is performed in Section 9. A detailed statistical significance analysis and associated determination of the upper limit for toroidal state cross section consistent with the present work is reported in Section 10.

5. Event Selection

Judicious choice of the experimental reaction exit channel is important for maximizing the likelihood of observing toroidal states. There is experimental suggestion and theoretical support for toroidal state breakup proceeding through complete α-disassembly [18, 17]. Heavy-ion collisions at this energy can have various reaction mechanisms which can depend on the impact parameter, including multifragmentation, nucleon transfer, incomplete fusion, and binary excited decay [34, 35, 36, 37]. Binary reaction mechanisms that give a highly excited projectile-like fragment are promising candidates for toroidal state production, as excitation energies up to ≈6 MeV/nucleon and angular momenta up to $96\hbar$ may be reached in this collision energy regime [28, 35]. The high event rate, duration of data collection, and adequate FAUST acceptance has yielded over an order of magnitude increase in measured 7-α events compared to previous work (186,097 FAUST events compared to 6,467 NIMROD events) [18]. Additionally, a total of 22,602 8-α events have been measured, allowing the α-disassembly of ^{32}S to be examined for possible toroidal states.

To gate on such events, it is important to exclude 7,8-α events that contain signatures of pre-equilibrium emission and target-like α-particles. The DADL detector thicknesses are well tuned to measure projectile-like particles; the punch-through energy of α-particles lies near the yield minimum between the predominantly target- and projectile-like contributions. The classification of 7,8-α events includes those where seven or eight α-particles are isotopically identified and coincidentally measured in FAUST. Further, such events that contain additionally measured Z = 1 particles are included, but the excitation energy is calculated excluding such particles (7-α: 56% contain at least one measured Z = 1 particle. 8-α: 45%). In keeping with ref. [18], α-particles are required to have no more than 40 MeV in the 7,8-α center of mass frame; the small number of events containing any α-particles outside of this region are excluded from the corresponding analysis.

6. Excitation Energy Analysis

A clear experimental observable for identifying charged-particle-decaying excited states is to look for correlations in the form of peaks in the excitation energy distribution for the decay channel of interest [38]. The excitation energy of the ^{28}Si(^{32}S) that leads to 7-(8-)α decay can be calculated by summing the center-of-mass kinetic energy of each α-particle and

subtracting the decomposition Q-value:

$$E_x = \sum_{i=1}^{M_{dp}} KE_{dp}^{com}(i) - Q \tag{1}$$

6.1. Efficiency and Resolution

When interpreting experimental excitation energy distributions for the study of nuclear excited states, it is important to understand the detector apparatus bias and efficiency. Given that toroidal high-spin isomer state excitation energies, widths, and possible existence is not well constrained, it is crucial to ensure that the FAUST detector energy thresholds, geometric acceptance, double-hit bias, and energy-dependent angular resolution does not produce artifacts in the excitation energy distribution that could be falsely interpreted as excited states. For this purpose, 7,8-α breakups were simulated and FAUST-filtered to obtain the detection efficiency as a function of the excitation energy as shown in panel (b) of Figure 1. To simulate breakups, the experimental laboratory velocity and θ distributions of the 7,8-α center-of-mass were sampled, the laboratory ϕ of the source was randomized, and α-particles were ejected at random angles with a velocity sampled from the experimental α-particle source frame distribution. The resulting ratio between the excitation energy distribution of simulated breakups before and after filtering exhibit no sharp features in regions of considerable yield for both 7- and 8-α events.

The width in the energy of a nuclear excited state decay is related to the lifetime of that state; thus, the ability to accurately measure decay energy widths provides key insight to the stability of the excited state [39]. Characterizing the expected resolution for an excited state decay measurement is necessary for untangling the convolution of the intrinsic state width and the detection resolution. To determine the expected resolution for such decays, excitation energy distributions can be generated after filtering decays of discrete excitation energy through the FAUST filter, which models the energy resolution, detector location uncertainty, and energy- and theta-dependent angular resolution of the array. To sample 7,8-α decays of discrete excitation energy where the individual α-particles retain similar laboratory energy and angular distributions, an event mixing procedure was used. To create a 7-α mixed event, an α-particle is randomly chosen in seven separate, randomly chosen experimental 7-α events. Mixed events containing two particles in the same detector telescope of FAUST were rejected. The measured energies and angles of each α-particle in the mixed event are then treated as the true values. The excitation energy of this mixed event is then calculated before (true) and after (smeared) filtering. This process is repeated for a large number of iterations. Gaussian fits are then performed on the smeared distributions for small regions of the true excitation energy and the resulting uncertainty (FWHM) is plotted as a function of the true excitation energy as shown in black in panel (a) of Figure 1. The same procedure was repeated for 8-α events as shown in red. In both cases, a roughly linear, positive correlation is established between the excitation energy and the resolution, which results from larger excitation energy breakups containing α-particles with greater energies; as the energy of the α-particle increases, the energy deposited in the DADL

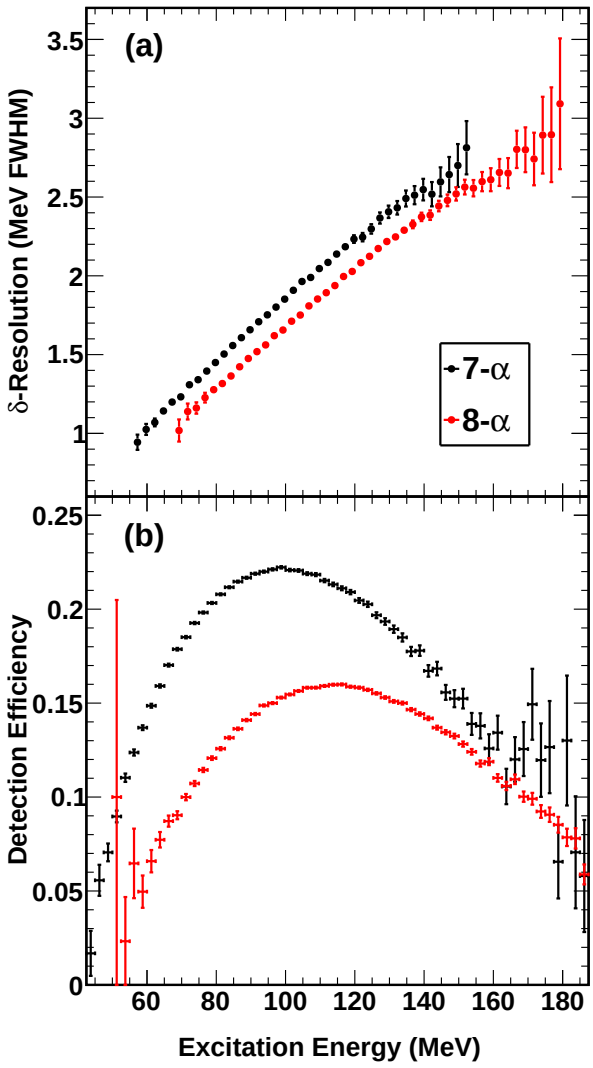

Figure 1: Monte Carlo simulation results for determining the resolution and detection efficiency of FAUST as a function of the excitation energy. Panel (a): Width (MeV FWHM) of the excitation energy distribution measured in FAUST for an infinitely narrow state for 7-α events (black) and 8-α events (red). These values indicate the Gaussian uncertainty to the excitation energy measurement. Error bars are obtained from the error in the Gaussian fits to the smeared distributions. Panel (b): Detection efficiency for simulated 7-α breakups (black) and 8-α breakups (red). The technique used for breakup simulation is described in the text.

detectors decreases, and the position (angular) resolution worsens. Additionally, as the excitation energy increases, a larger fraction of α-particles will be measured at larger θ_{lab} angles where the FAUST detectors cover a larger solid angle, giving worse angular resolution. For a simulated narrow resonance at 140 MeV excitation energy, the work of ref. [18] reported that the observed experimental width in NIMROD would be ≈9.5 MeV FWHM; in comparison, an equivalent FAUST measurement is expected to have a ≈2.5 MeV FWHM.

6.2. Excitation Energy Distributions

The excitation energy for each measured 7,8-α event is calculated using Equation 1 and the distributions are shown in panels (a,b) of Figure 2. The excitation energy range of the measured 7-α distribution is consistent with that measured in ref. [18]; however, a slight difference in the overall shape is observed due to detection efficiency differences between NIMROD and FAUST. Yield associated with any appreciably produced resonances would show up as finer peak-structures above the smooth continuum. Qualitatively, there are no discernible strong resonances in the 7-α spectrum; in comparison, the 8-α spectrum shows minor fluctuations that could possibly indicate correlated yield, although this spectrum has significantly lower counts and requires closer quantitative analysis to determine if these are statistically significant. To produce a background distribution that well-describes non-resonant contributions to the spectrum, many works (including the NIMROD 7-α work of ref. [18]) invoke the event mixing technique [40, 41]. This method provides a potential avenue for producing uncorrelated background spectra a priori while retaining experimentally measured

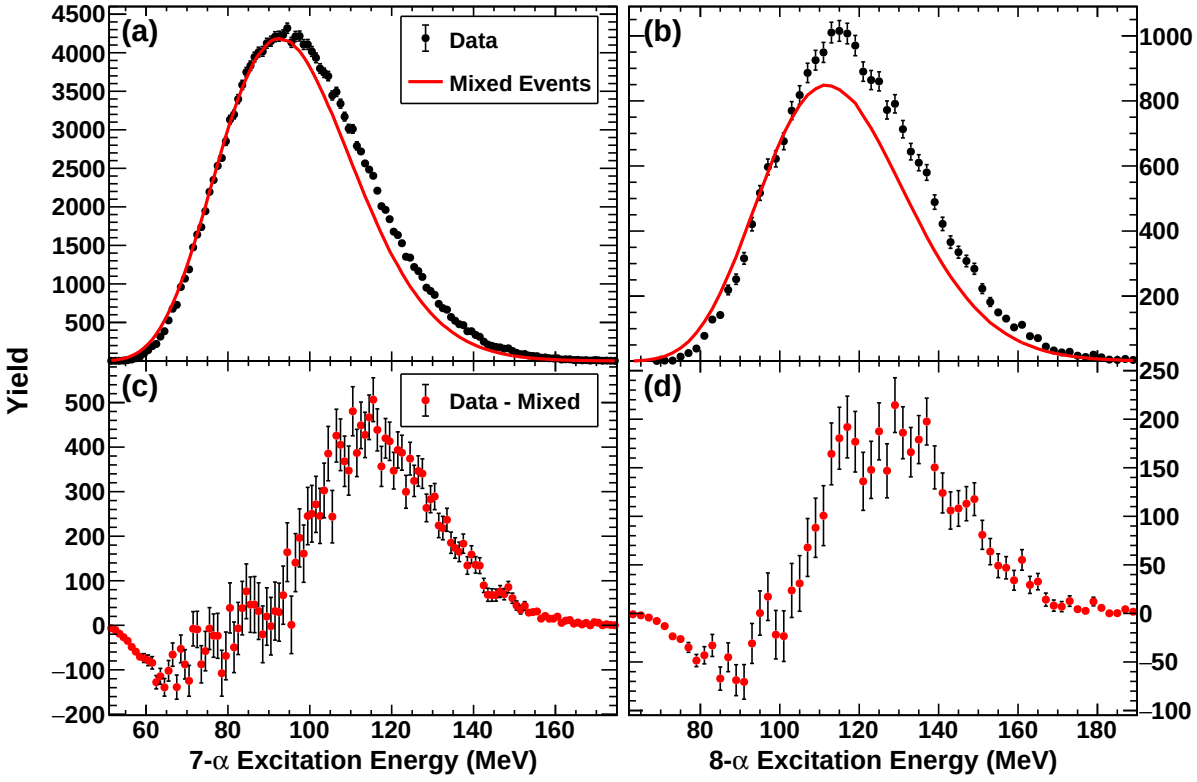

Figure 2: Excitation energy distributions and mixed event subtraction for measured 7,8-α events. Panel (a,b): Experimental 7-α (a) and 8-α excitation energy distribution with 1 MeV and 2 MeV bin widths, respectively. The mixed event background (red line) is normalized to the experimental distribution as described in the text. Panels (c,d): Residual spectrum after subtracting the mixed event distribution from the experimentally measured distribution.

single particle energy and angular distributions.

For this analysis, the event mixing technique as described in Section 6.1 was performed 200 times per measured event to ensure that the resultant background distribution is largely free of statistical fluctuations. It is important to keep in mind that mixed events do not contain Coulomb repulsion effects that exist in the experimental data, giving a higher probability for producing events with lower excitation energy than exists for experimental data. Normalization of the mixed event distribution to the experimental distribution should ideally not be performed in a region significantly impacted by this Coulomb discrepancy or where resonant contributions are expected to occur. Given this, the normalization was performed from 70 to 96 MeV for 7-α events and from 91 to 107 MeV for 8-α events. Subtraction of the normalized mixed event distribution from the experimental distribution for 7-α events as seen in panel (c) shows similar gross features to previous work, including a Coulomb-caused yield deficit at low excitation energy (≈70 MeV) and a broad yield excess at higher

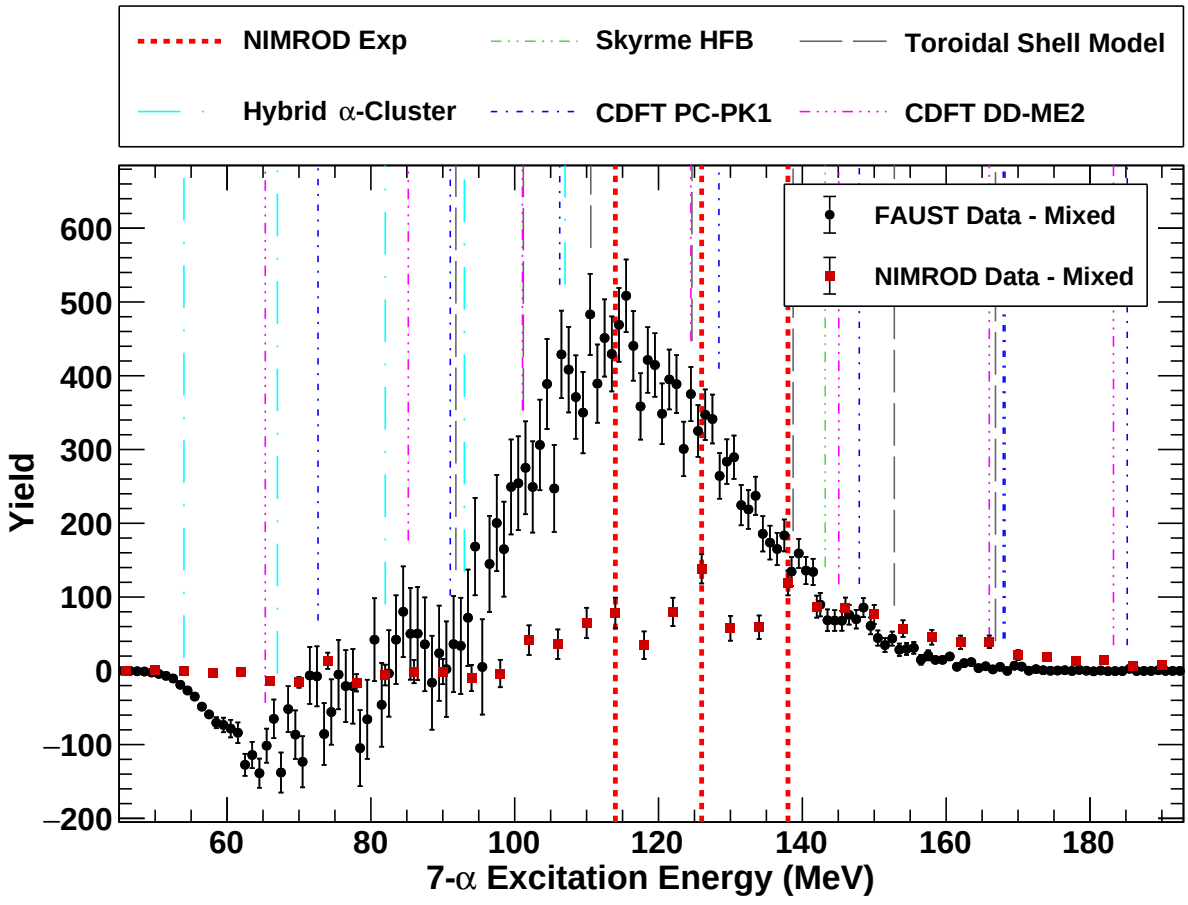

Figure 3: Subtracted 7-α excitation energy distribution from the current work (black circles) compared to previous work (red squares, red dashed vertical lines) and theoretical predictions of toroidal high-spin isomers in ^{28}Si (vertical lines) [21, 18, 17, 14]. States from ref. [21] with significant broadening and overlap are not reproduced in this figure, as experimental sensitivity is not expected.

excitation energy (≈115 MeV). The broad excess was previously interpreted to originate entirely from multiple toroidal states [18]. While the same general features are seen for the subtracted 8-α spectrum in panel (d), the normalized mixed events fail to describe the data in the normalization region. It is possible this arises from the Coulomb contribution being more significant due to the additional α-particle, affecting a larger range of excitation energy. Further discussion about the validity of the mixed event technique in this framework is given in Section 6.3.

The residual spectrum from panel (c) of Figure 2 is reproduced in Figure 3 and overlaid with both the data from ref. [18] and all predicted toroidal state means of various calculations to compare results. By comparing the current data with the locations of states reported in the NIMROD experiment, no strong signature for states at these energies is present in the current data set, despite significantly improved statistics and resolution of measurement. If the mixed event background description is assumed to be accurate, the presence of broad overlapping state contributions to explain the yield excess cannot be ruled out, although the width of such states would be too large to be consistent with the NIMROD measurement. While the presence of finer peak structure may be seen in a few regions (e.g., ≈ 87 and ≈148 MeV), lack of predictive power in the various theoretical calculations — as evidenced by the various vertical lines spanning the entire distribution — makes attributing such subtle features to a toroidal state exceptionally challenging [21, 18, 17, 14]. A potential peak nearly anywhere in the distribution could be reasonably attributed to a predicted state, highlighting the importance of exercising caution when using such predictions as guidance.

6.3. Background Description

The event mixing technique, sometimes referred to as the "combinatorial background", is used extensively for producing uncorrelated background descriptions in the high energy regime of nuclear particle physics [42]. This technique has also been used in a number of intermediate energy heavy-ion collision analyses [43, 40]. Under ideal circumstances, event mixing carries the benefit of allowing broad and overlapping state contributions to be extracted from the total measured spectrum. However, it has been found that careful requirements and constraints to mixed event kinematic properties can be important for producing an accurate background [44, 40]. The broad excess of yield seen in panel (c) of Figure 2 motivated the addition of kinematic requirements to the event mixing procedure to see if reasonable constraints could produce a background description that captures the entire experimental distribution. To this end, various mixing constraints were attempted, including only mixing between events of similar reconstructed source velocity, only mixing between events of similar excitation energy, or both constraints simultaneously. Further, using the center-of-mass frame velocity vectors calculated in each of the randomly chosen α-particles real measured event center-of-mass frame rather than using the laboratory frame velocities was attempted. For this treatment, constraints to the center-of-mass angles between α-particles in the mixed events were included to prevent choosing multiple α-particles emitted at similar angles. In every case, the produced mixed event background description was shifted to lower mean excitation energies than the unconstrained procedure, failing to agree

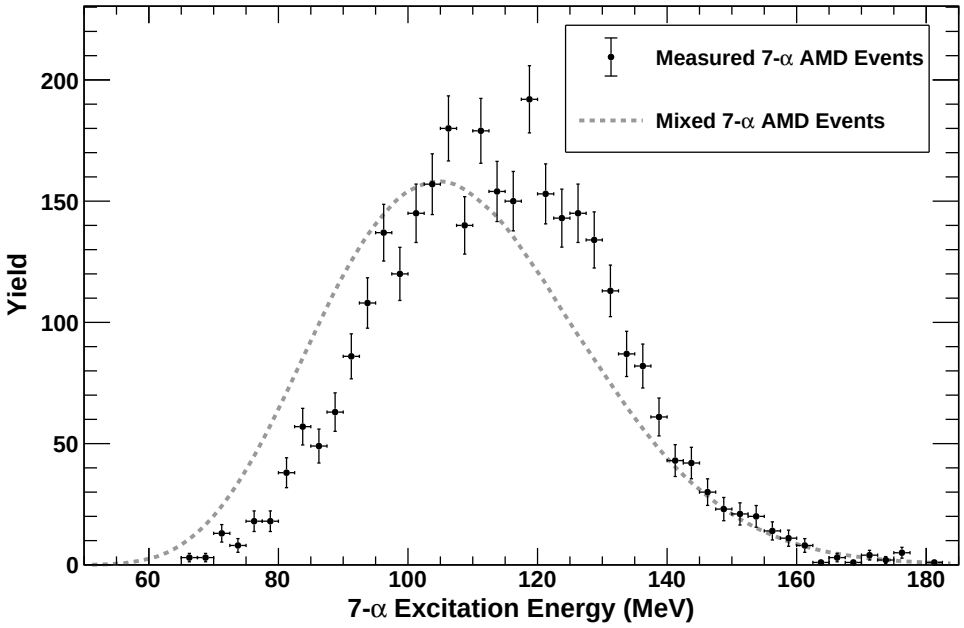

Figure 4: Filtered AMD + GEMINI++ simulated excitation energy distribution for 7-α events (black circles). The distribution obtained after performing the event mixing technique is shown by the gray dashed curve. The mixed event distribution is normalized to the measured distribution to give equal total integrals.

with the experimental distribution in any region; after subtraction, there is even greater enhanced yield deficits at lower excitation energies and yield excesses at higher excitation energies.

The inability to reasonably produce a mixed event background that well describes the grossly smooth, single-peaked experimental 7-α distribution motivated the exploration of alternative background generation procedures. The anti-symmetrized molecular dynamics (AMD) model was developed to simulate heavy-ion collisions in the intermediate energy regime [45, 46]. Comparison of collision properties and observables between AMD and experimental data give excellent agreement [47, 48]. Although AMD models the complex dynamics of nuclear collisions with exceptional detail, it does not accurately model resonant state particle-particle correlations, and so the excitation energy distribution for 7-α events produced in the simulation is expected not to contain any resonance contributions. Reasonable calculation time yielded 1,600,000 ^{28}Si + ^{12}C AMD collisions at 35 MeV/nucleon simulated out to 300 fm/c. The nuclear fragments produced in AMD collisions contain excitation energy and must undergo de-excitation according to available pathways. For this purpose, a statistical decay code (GEMINI++) is paired with AMD to produce the final state reaction products for each collision [49]. Each AMD collision was coupled to GEMINI++ once (some other work runs GEMINI++ many times per AMD collision to bolster limited AMD statistics). For the remainder of this work, figures labeled with "AMD" refers to the pairing of AMD and GEMINI++.

The 7-α excitation energy distribution for filtered AMD + GEMINI++ events is shown

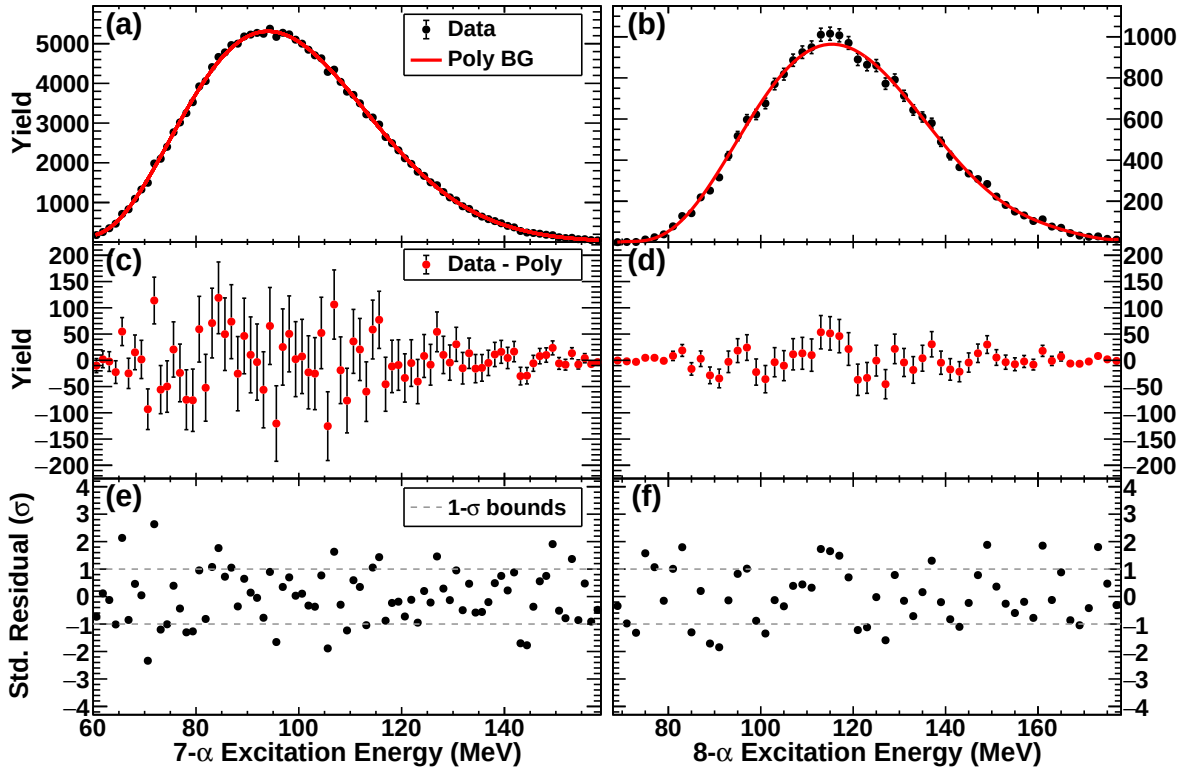

Figure 5: Excitation energy distributions and background continuum descriptions using polynomial fits. Panel (a,b): Experimental 7-α (a) and 8-α excitation energy distributions in 1.25 MeV and 2 MeV wide bins respectively. A polynomial of 9^{th} (a) and 7^{th} (b) order are fit to the data as shown by the red curves. Panels (c,d): Residual spectra after subtracting the polynomial fits from the experimentally measured distributions. Panels (e,f): Standardized residual plots obtained by dividing the data in panels (c,d) by the square root of the expected count error of the fits. Horizontal dashed lines are drawn to indicate the 1-σ region.

in Figure 4. The shape of this distribution is qualitatively similar to the experimental data; however, the mean is ≈15 MeV greater. This similar discrepancy was observed in ref. [18] where the AMD + GEMINI++ distribution was shifted down in excitation energy to agree with experiment. Nevertheless, if the mixed event procedure is a valid way to produce a background description for these 7-α events, event mixing of the simulated data should agree with the event-by-event excitation energy distribution. The distribution obtained by performing event mixing on the filtered simulation data is shown by the gray dashed curve in Figure 4. For this study, no energy or angular smearing was performed by the filter. Nevertheless, the distribution obtained from event mixing does not match the measured distribution. If this mixed event distribution was normalized to the measured distribution in an analogous range as Figure 2 and subtracted, a similar deficit and excess of yield would be obtained. While the Coulomb interaction likely plays a role in this discrepancy, it is unlikely to explain the deviation in shape at higher excitation energies ($>$ 100 MeV). Typically, event mixing is applied to particle correlations that are a relatively small subset of the total

collision system and thus there is little precedent for applying such a technique for describing background contributions where the correlation of interest contains most of the mass of the system. These observations raise concern in the application of the mixed event technique for this class of events.

Given the observed shortcomings of the mixed event technique in this context, an alternative approach for assessing the statistical significance of any fluctuations is essential. For many experimental resonant state studies, there is significant yield, narrow measured width, and confidence in the predicted decay energy. In this case, the error introduced in roughly describing the background with a smooth polynomial does not impede the extraction of state properties [50, 51]. Locating yield associated with excited state resonant decay relies on determining whether any features of the experimental distributions deviate from expected fluctuations of a smooth continuum. To phenomenologically produce a continuum that well describes the entire range of the excitation energy distribution, the experimental 7-α data is fit with a 9^{th} order polynomial, producing a smooth, single-peaked background as shown in panel (a) of Figure 5. The order of the polynomial was chosen by finding a minimum in the χ^2/ν for polynomials of order 4 through 11 and ensuring that the resulting fit was unimodal and described the gross shape of the experimental data. Just as in Figure 2, the polynomial background was subtracted from the experimental data, leaving the residuals in panel (c). As the count error scales with the square root of the number of counts, larger error bars in the residual correspond to larger absolute yield in the data. One way to account for the changing relative error across the distribution is to instead plot the standardized residual as shown in panel (e), where the residual values in panel (c) are divided by the expected count error of the fit. If the data is well described by the produced background, the standardized residual data is expected to obey Gaussian populations, with ≈68.2% of the data lying between -1σ and 1σ, ≈27.2% of data lying between $\pm$(2σ and 3σ), ≈4.2% of data lying between $\pm$(3σ and 4σ), and so on. In other words, the data in panel (e) projected to the y-axis will give a Gaussian distribution centered at 0 with a standard deviation of 1σ if the background well describes the underlying distribution. The χ^2/ν of the fit indicates the width of this projected distribution and has a value of 1.01 for the 7-α data. The calculated χ^2/ν can be compared to the corresponding χ^2 distribution (which depends on the number of degrees of freedom, ν). Integration of this distribution to the right of the measured χ^2/ν yields a p-value, indicating the probability that the measured distribution with the given fluctuations would happen by chance (p = 0.44 for the experimental 7-α distribution with this assumed background). The ubiquitously used standard for a statistically significant p-value is p = 0.05, well below what is seen here. The standardized residuals also show a qualitatively random deviation from the mean with no apparent structure. It is important to note that this statistical analysis loses sensitivity as the width of possible states increases and the yield decreases, as at some limit such features will drive the fit to describe them. The same procedure was performed using a 7^{th} order polynomial for 8-α events in panels (b,d,f) of Figure 5, giving a χ^2/ν of 1.17 with an associated p-value of 0.22. While the two residual spectra in panels (d,f) may show subtle structure, none of the features deviate substantially from the expected distribution or agree with the ≈154 MeV predicted state in

^{32}S [14]. Further statistical significance analysis and discussion can be found in Section 10.

7. Sequential vs. Simultaneous: Decay Intermediates

The mechanism of decay for highly excited nuclei can be largely categorized into two extremes: successive binary decays (sequential) and prompt multifragmentation (simultaneous). The simultaneous decay scenario is typically used to describe a fast mechanism where the colliding nuclei "explode" into many fragments [52, 53]. The dominant decay mode has been found to depend largely on the excitation energy of the decaying nucleus, in which the simultaneous mechanism becomes favorable at higher excitation energies (>3 MeV/nucleon) [54, 53]. There is limited theoretical support for the predicted decay timescale (lifetime) and mechanism of a clustered toroidal high-spin isomer. Given the high excitation energy, large angular momentum, ring-like structure, and predicted stability of such states, it is reasonable

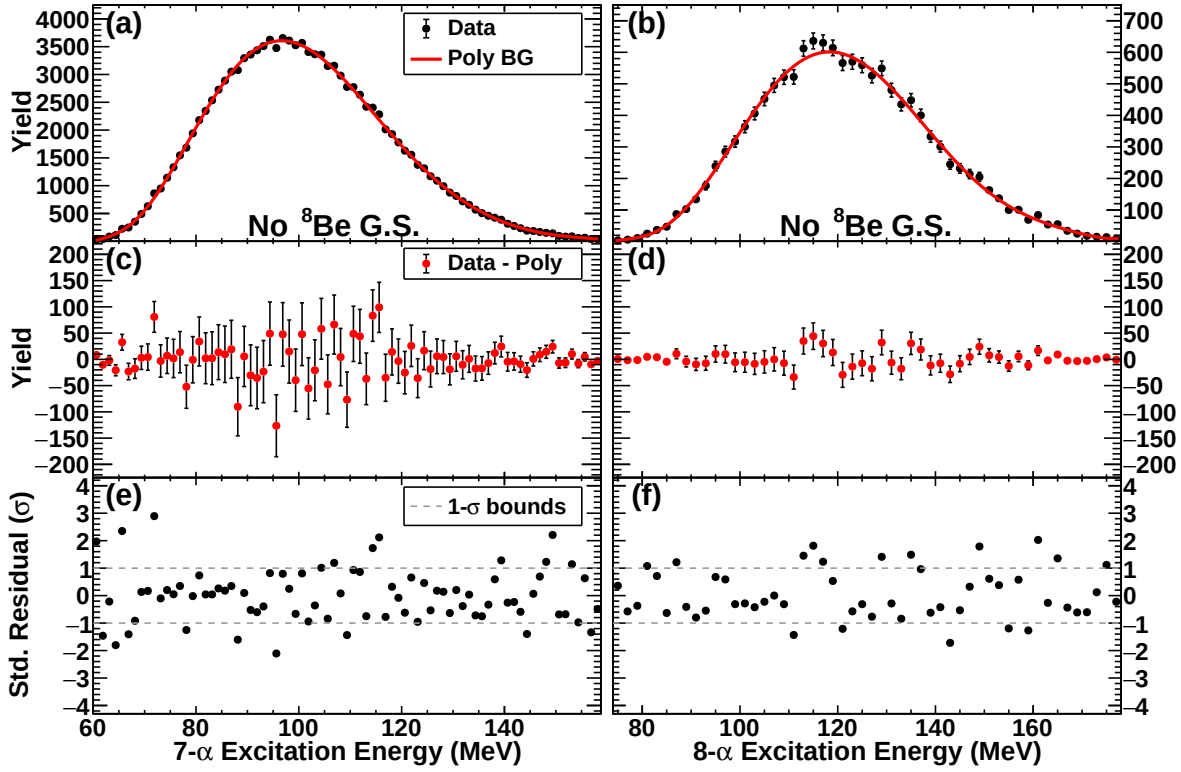

Figure 6: Excitation energy distributions for 7,8-$\alpha_{NoG.S.}$ events with background continuum descriptions using polynomial fits. Panel (a,b): Experimental 7-$\alpha_{NoG.S.}$ (a) and 8-$\alpha_{NoG.S.}$ (b) excitation energy distributions in 1.25 MeV and 2 MeV wide bins respectively. A polynomial of 9$^{\text{th}}$ order are fit to both sets of data as shown by the red curves. Panels (c,d): Residual spectra after subtracting the polynomial fits from the experimentally measured distributions. Panels (e,f): Standardized residual plots obtained by dividing the data in panels (c,d) by the square root of the expected count error of the fits. Horizontal dashed lines are drawn to indicate the 1-σ region.

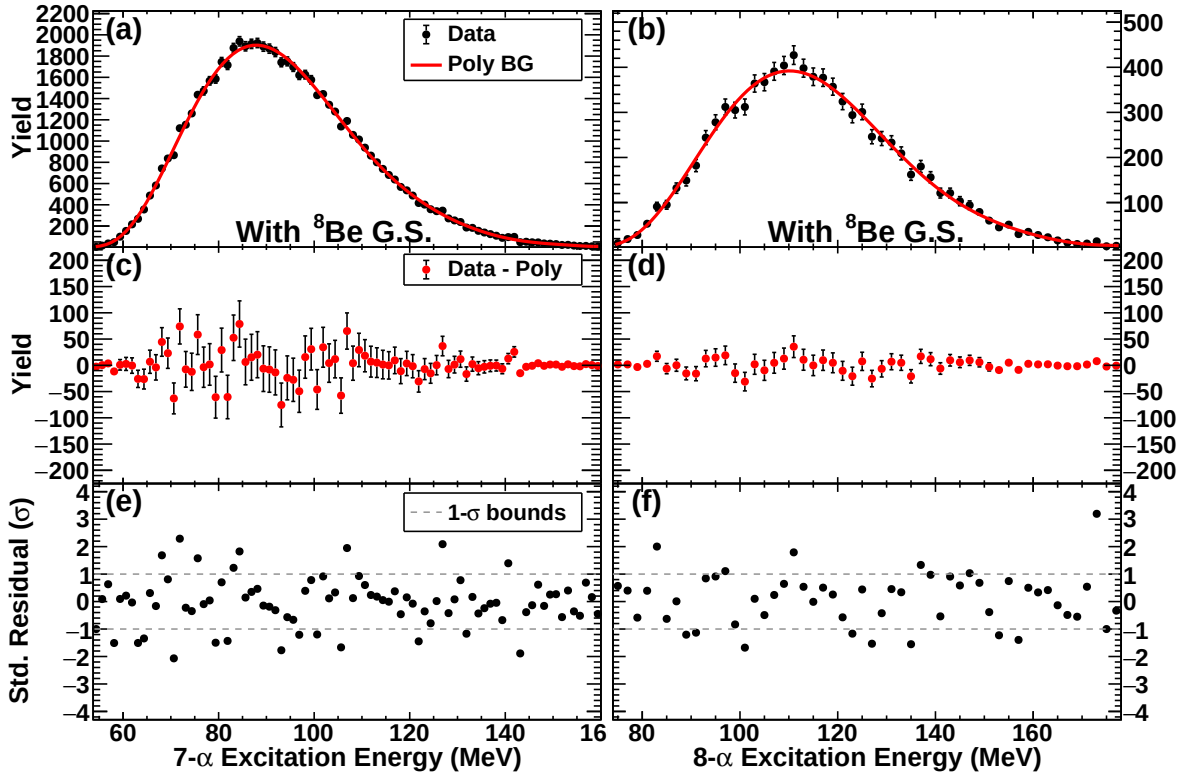

Figure 7: Excitation energy distributions for 7,8-$\alpha_{WithG.S.}$ events with background continuum descriptions using polynomial fits. Panel (a,b): Experimental 7-$\alpha_{WithG.S.}$ (a) and 8-$\alpha_{WithG.S.}$ (b) excitation energy distributions in 1.25 MeV and 2 MeV wide bins respectively. A polynomial of 11^{th} (a) and 9^{th} (b) order are fit to the data as shown by the red curves. Panels (c,d): Residual spectra after subtracting the polynomial fits from the experimentally measured distributions. Panels (e,f): Standardized residual plots obtained by dividing the data in panels (c,d) by the square root of the expected count error of the fits. Horizontal dashed lines are drawn to indicate the 1-σ region.

to consider the possibility of simultaneous decay enhancement even over longer timescales. One way the degree of simultaneity is characterized in experimental data is by simulating each decay mechanism extreme and comparing the model results to various breakup observables (e.g, source frame relative angles and kinetic energy spectra) [55, 56]. A more selective technique involves identifying sequential breakups on an event-by-event basis by observing intermediate unbound excited states [57]. To select on 7,8-α events that decay through the ^{8}Be ground state, the excitation energy distribution for all combinations of two α-particles was produced for each class of events and a gate was placed around the ground state peak. If any 7,8-α events proceed through a simultaneous decay mechanism, the ensemble of data that does not include the ^{8}Be ground state (and, by extension, excited states of ^{12}C* and ^{14}O* that are known to decay through the ^{8}Be ground state) will contain a higher fraction of such events [58, 51].

A main objective of partitioning 7,8-α events into 7,8-$\alpha_{WithG.S.}$ and 7,8-$\alpha_{NoG.S.}$ is to

increase the possible resonant state yield to background yield ratio. While the work of ref. [18] indicates that the bulk 7-α breakup properties are consistent with a sequential decay mechanism, the mechanism for possible toroidal high-spin state breakup remains an open question which, if present, would only constitute a small fraction of the data. As in Section 6.3, the 7,8-α excitation energy distributions can be examined for statistically significant yield enhancements. The same treatment of the data as for Figure 5 is performed for 7,8-$\alpha_{NoG.S.}$ events as shown in Figure 6. While there is some indication of overfitting, as evidenced by the regions of excitation energy with similar and small standardized residuals in panels (e,f), the polynomial fit is still a unimodal description of the data and does not contain any perceivable fluctuations. There is no indication of resonant state yield outside of expected fluctuations (7-α: p = 0.73, 8-α: p = 0.52). The slight enhancement seen at $\approx$115 MeV in panel (f) does not agree with the predicted $\approx$154 MeV state and is otherwise below the threshold for making any significant claims. The same analysis is performed for 7,8-$\alpha_{WithG.S.}$ events as shown in Figure 7. The standardized residual plots in panels (e,f) also do not show any evidence of strong resonant state yield (7-α: p = 0.20, 8-α: p = 0.47).

8. Momentum Shape Analysis

Momentum shape analysis is a way to characterize the emission pattern, reveal details of the reaction dynamics, provide insight to decay timescales, and study collective flow for particles produced in heavy-ion collisions at intermediate and relativistic energies [59, 60]. For examining the properties of 7,8-α decays, the two main properties of interest are the sphericity and coplanarity. If a toroidal high-spin isomer decays through a simultaneous mechanism into fragments of equal mass, the momentum shape distribution would be directly related to the geometric configuration at breakup and thus such breakups could be expected to have enhanced coplanarity. On the other hand, the relationship between momentum shape and configuration space becomes increasingly indeterminate for sequential decays. The momentum shape analysis uses a tensor constructed from the product of all α-particle momenta and can be written as:

$$T_{i,j} = \Sigma_{\nu=1}^{N} p_i^{\nu} p_j^{\nu} \tag{2}$$

where N is the total number of α-particles, p_i^{ν} is the momentum component of the ν^{th} particle in the center-of-mass frame, and i refers to the Cartesian coordinate. Diagonalizing the tensor reduces the overall momentum shape to an ellipsoid. Qualitative shape information about each event is obtained using the normalized and ordered tensor eigenvalues, λ_1, λ_2, and λ_3. The sphericity of the momentum shape is defined as $S = \frac{3}{2}(1 - \lambda_3)$, and the coplanarity is defined as $C = \frac{\sqrt{3}}{2}(\lambda_2 - \lambda_1)$. This defines a sphericity-coplanarity space bound by a triangle with (S, C) vertices of $(0, 0)$, $(3/4, \sqrt{3}/4)$, and $(1, 0)$, corresponding to the extreme shape cases of entirely rod-like, disk-like, or sphere-like, respectively. Momentum shape information becomes increasingly well defined with increasing number of particles in the tensor. In the case of two or three particles, all data will lie along the rod-disk axis. Sphericity-coplanarity distributions for AMD + GEMINI++ filtered 7-α events and experimental 7,8-α events are shown in Figure 8. There is qualitative agreement between

all three distributions with the peak of the data located between all shape extremes and the mean coplanarity of each distribution being comparable. The same agreement was found in ref. [18] as it was discovered that the characteristics of the AMD + GEMINI++ shape distribution is largely dictated by the GEMINI++ sequential decay code; simulated events that give seven α-particles in the exit channel typically only have a few excited primary fragments fed to GEMINI++ from AMD at $t = 300$ fm/c. Like in this previous work, there is no indication of enhanced coplanar yield in the experimental distributions compared to simulation.

The lack of strong evidence for toroidal high-spin isomers in the excitation energy yield distributions prompts the exploration of other observables potentially sensitive to their existence. The mean sphericity and coplanarity as a function of excitation energy for 7,8-α events is shown in Figure 9. For both 7- and 8-α events, the mean sphericity and coplanarity decrease as the excitation energy increases. In other words, as the excitation energy increases, the shape of the α-particle momenta becomes elongated on average. These trends are well reproduced by the AMD + GEMINI++ simulation data for 7-α events (8-α event simulation results are excluded due to poor statistics). This relationship between the momentum shape observables and excitation energy may provide further insight to the nature of α-disassembly in these collisions, as both observables are related to the timescale and mechanism for decay. Model calculations of prompt multifragmentation typically yield significantly higher mean sphericity and modestly higher coplanarity than that obtained using sequential decay models [60, 61, 62]. However, as discussed in Section 7, prompt decays are thought to become favored for sources with higher excitation energies. The trends seen in Figure 9 show the opposite trend from what would be expected in a scenario of prompt breakup. Given that the experimental trend is reproduced by simulation and that most simulated 7-α events come from the sequential de-excitation of a few dynamically produced primary fragments, is is unlikely that all the 7-α events come from a de-exciting ^{28}Si source.

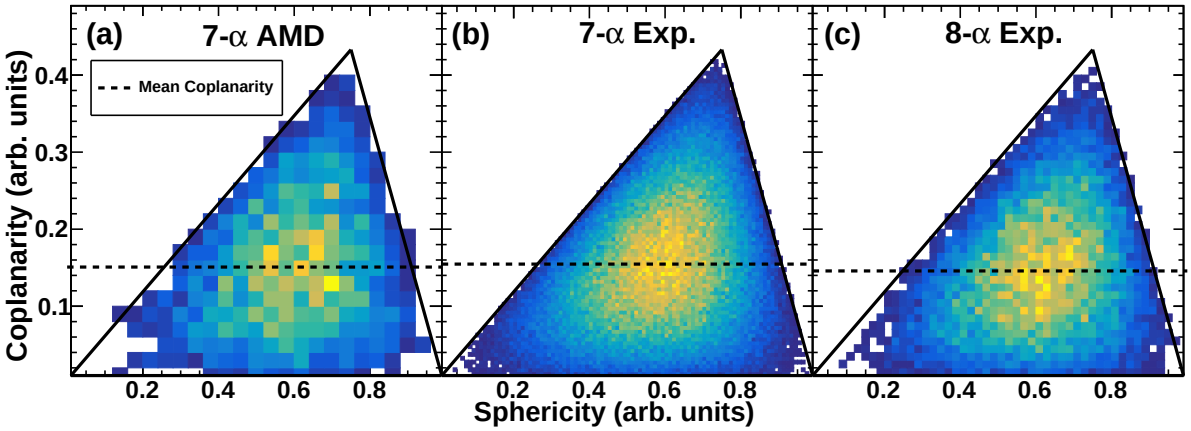

Figure 8: Simulated and experimental momentum shape sphericity-coplanarity yield distributions with a linear color scale. The mean coplanarity for each panel is shown by the horizontal black dashed line. Panel (a): Shape distribution for AMD+GEMINI++ filtered 7-α events. Panel (b): Experimental 7-α data. Panel (c): Experimental 8-α data.

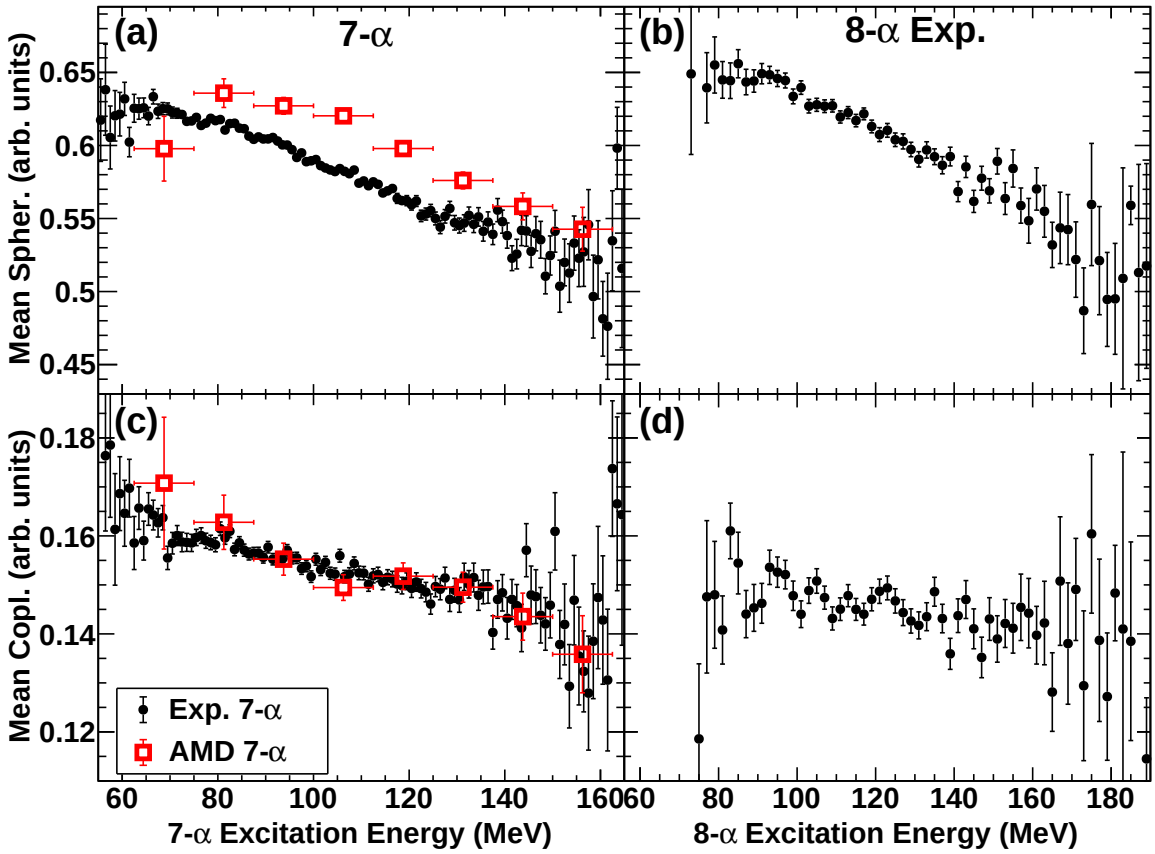

Figure 9: Mean sphericity and coplanarity as a function of excitation energy for 7,8-α events. Panels (a,b): Experimental sphericity dependence for 7-α (a) and 8-α (b) events (black circles). Panels (c,d): Same as panels (a,b) but for the mean coplanarity dependence. The filtered AMD + GEMINI++ results (red open squares) are overlaid for 7-α events in panels (a,c).

Authors of ref. [63] have demonstrated the difficulty in isolating clean projectile decay samples in collisions of ^{40}Ca + ^{40}Ca at 35 MeV/nucleon due to the dynamics at the early stages of the collision leading to detected α-conjugate exit channels. It was found that in these α-conjugate decay channels, a hierarchical effect is seen in the projectile-like decay products; on average, heavier α-conjugate fragments have larger beam-component velocities than the lighter fragments. This indicates that a significant portion of α-particles in such channels emerge from the low density overlap region in the early stages of the collision [64]. These particles are still projectile-like enough to pass the event selection in this work and are difficult to exclude due to the broad phase space they inhabit; in this previous work, the parallel velocity distributions do not show distinguishable features in α-disassembly events to permit isolation between the two α-particle sources. It is likely that the origin of many 7-α events is best understood as some portion of α-particles originating from dynamical interactions early in the collision and the remaining originating from a heavier, faster α-conjugate source disassembly. In such cases, the misidentified common center-of-mass reference would lie between

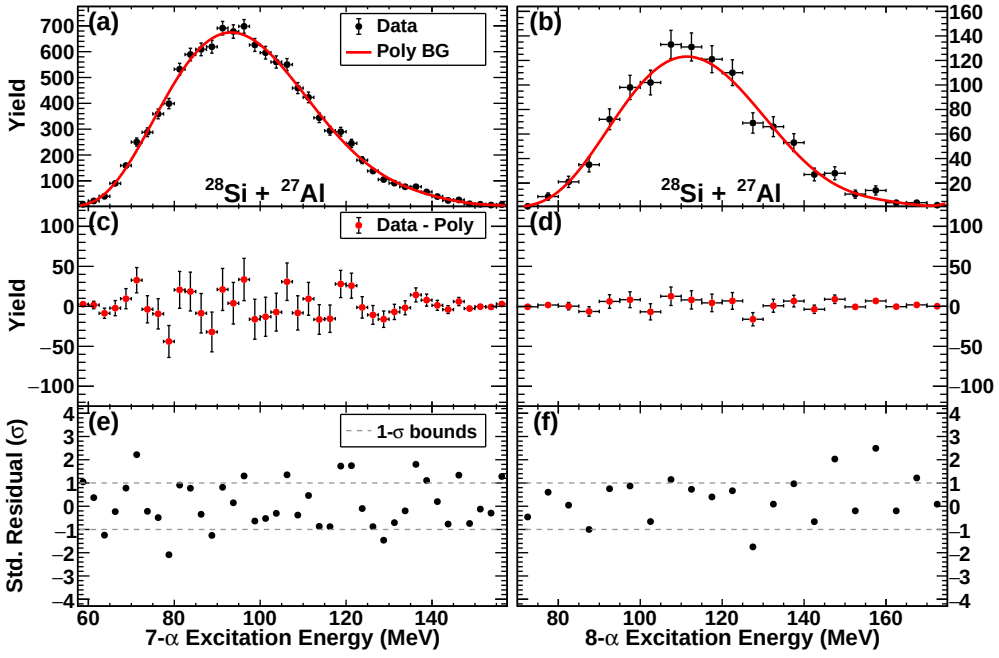

(a) ^{28}Si + ^{27}Al at 35 MeV/nucleon.

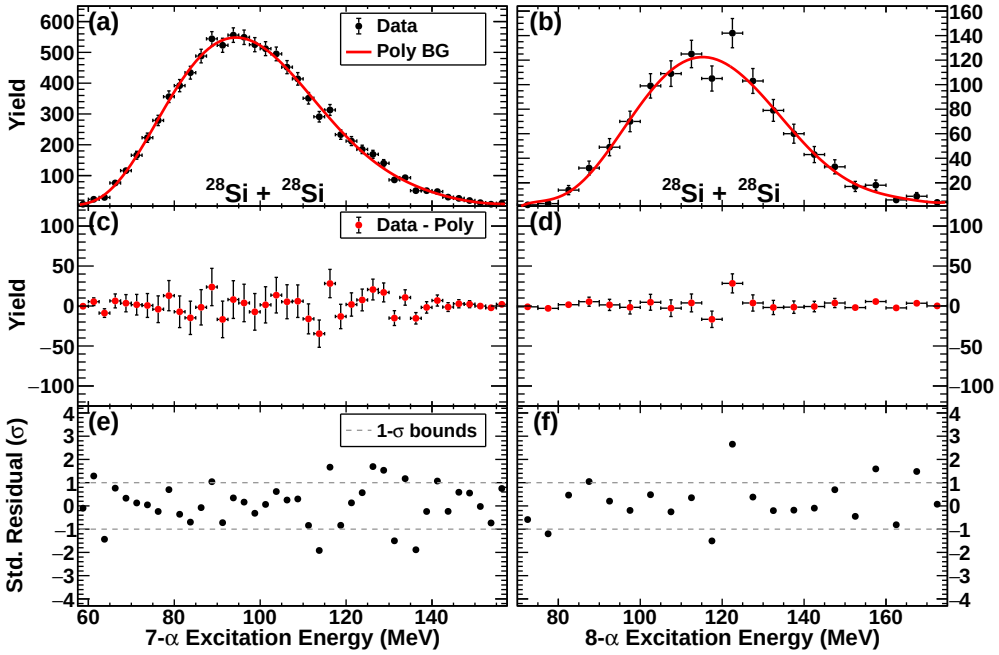

(b) ^{28}Si + ^{28}Si at 35 MeV/nucleon.

Figure 10: Analogous excitation energy analysis procedure for 7,8-α events as in Figure 5 but for ^{27}Al and ^{28}Si targets.

these two distinct "sources", leading to an artificially higher calculated excitation energy and a seemingly elongated momentum shape of breakup. This proposed interpretation is further supported by the AMD + GEMINI++ simulation agreement with the experimental shape-excitation energy trends. AMD is capable of modelling the complex dynamics of early collision stages. Given that the simulated events that result in seven measured α-particles in the exit channel originate from the sequential de-excitation of a few excited fragments produced in the dynamical stage of the collision, the same common center-of-mass misidentification is likely to occur.

9. Target Size and α-Conjugation

The choice of a ^{12}C target for the collision system was largely to replicate the experimental conditions of ref. [18]. As the role of the target is primarily to provide a means of exciting the projectile during the collision, it is of interest to explore if alternative target species may enhance toroidal high-spin isomer production. The authors of ref. [21] have also proposed that symmetric collisions of ^{28}Si + ^{28}Si may enhance such production, as only even l-values are admitted in the entrance channel. As a direct comparison to the symmetric collision scenario, data was also obtained using a similar mass, non-α-conjugate ^{27}Al target. The same analysis procedure as performed for Figure 5 was used with the ^{27}Al and ^{28}Si target data as shown in Figure 10. As this study is largely exploratory, less data collection time was devoted to the study of these collision systems. Nevertheless, inspection of the 7,8-α event excitation energy distributions and associated standardized residuals for each collision system reveal similar agreement between the data and a smooth, unimodal continuum description (^{27}Al Target: 7α p = 0.19, 8α p = 0.24. ^{28}Si Target: 7α p = 0.44, 8α p = 0.43).

10. Statistical Significance Analysis and Upper Limit on Toroidal Cross Section

Although no obvious peaks are observed in the 7-α excitation energy distribution measured in FAUST, it is not possible to completely rule out the presence of states that are either too low yielding, too broad, or some combination that results in yield enhancement below statistical fluctuations. Confidently claiming the measurement of a resonance in this data depends on the state's cross section (corrected for FAUST detection efficiency), intrinsic width (convolved with FAUST resolution), and yield relative to background (accounting for background determination uncertainty). By reasonably accounting for these factors and assessing a limit of statistical significance for obvious peaks in the excitation energy distribution, an approximate toroidal high-spin isomer cross section upper limit in the 7-α exit channel can be obtained. The procedure for simulating 7-α excitation energy spectra with resonant yield and the simulation of expected experimental results consistent with previous measurement is discussed in Section 10.1. A statistical likelihood analysis for determining upper limits on toroidal state cross sections that can be compared to previous measurement is discussed in Section 10.2.

10.1. Simulated FAUST-Measured 7-α Spectra

As discussed in Section 1, authors of ref. [18] used AMD + GEMINI++ simulations to approximate cross sections of the observed high excitation energy states as seen in Table 1. Repeating the same procedure used in the prior experiment allows for a direct comparison between the two results. As neither the NIMROD nor FAUST experiment were designed for accurately measuring cross sections, there exists significant systematic uncertainty in the conversion from measured yield to cross section; however, when using the same procedure, the systematic error should be, to a great extent, the same. To this end, the 7-α decay cross section to measured yield conversion for the FAUST data was obtained by first interpolating the systematic parameterization of heavy-ion collision properties of ref. [28] to estimate a total cross section of 2417 mb for collisions of ^{28}Si + ^{12}C at 35 MeV/nucleon. It is then assumed that the total number of detected events in FAUST, corrected by the detection efficiency for measuring at least one particle, represents this total cross section. This total event detection efficiency was determined from the ratio between all AMD + GEMINI++ simulated collisions and those where at least one particle was measured after filtering; approximately 79% of AMD + GEMINI++ collisions have at least one particle measured in FAUST. The 7-α channel detection efficiency was found in a similar way; for AMD + GEMINI++ events that had at least seven projectile-like α-particles, the yield ratio of unfiltered to filtered events where seven α-particles were measured give a 7-α detection efficiency of $\approx$21%. These efficiency corrections allow for the relative frequency of measured resonant 7-α yield to all 7-α events ($\nu_{res.}$) to correspond to a cross section for the state ($\sigma_{res.}$); for FAUST, this conversion factor is $\sigma_{res.} = 52.0 \cdot \nu_{res.}$, where $\nu_{res.}$ is expressed as a percent.

The results in Section 6.3 demonstrated that the experimental 7-α distribution is well described by a smooth, unimodal background description. While the 9$^{\text{th}}$ order polynomial previously used aptly provided a continuum background description for most of the excitation energy range of the data, this functional form struggles to accurately capture the tails of the distribution where the yield approaches zero. To compensate, kernel density estimation (KDE) can be used to effectively smooth the measured 7-α distribution, providing a reasonable underlying probability density function given the finite data sample [65]. Unlike a polynomial, KDE guarantees that the resulting distribution is normalizable, is always non-negative, and contains tails that approach zero. A kernel density estimation of a discrete data sample can be expressed as:

$$f_h(x) = \frac{1}{n} \sum_{i=1}^{n} K_h(x - x_i) \tag{3}$$

where n is the number of discrete data points, K_h is the kernel function used at each data point with h bandwidth, and x_i is the x-value for each data point. A Gaussian distribution is chosen as the kernel for this work with the bandwidth h representing the standard deviation. A KDE generated using a bandwidth of 2 MeV produces a good description for the experimentally measured 7-α excitation energy distribution as shown by the agreement between the red line and black experimental data in panel (a) of Figure 11. By sampling the KDE distribution once for every experimentally measured 7-α event, a simulated distribution

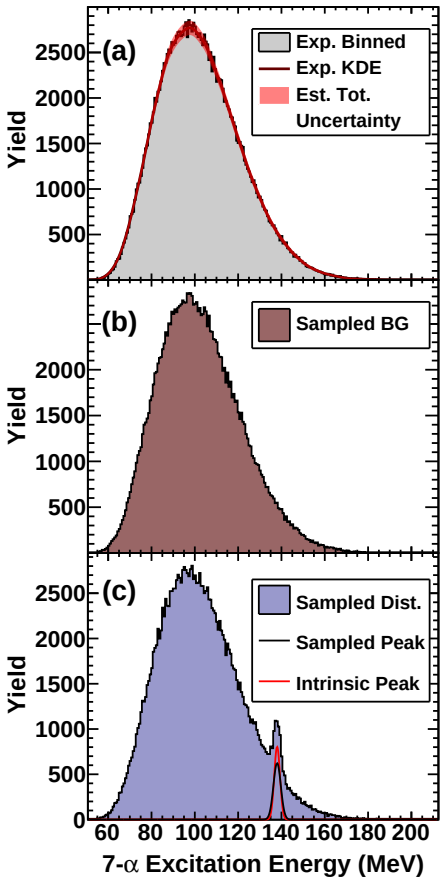

Figure 11: FAUST-simulated 7-α excitation energy distributions. Panel (a): Experimentally measured 7-α excitation energy distribution with the associated kernel density estimation (KDE) probability distribution (red line). The motivation and application of the shaded uncertainty region is discussed in the text. Panel (b): Simulated 7-α distribution produced from sampling the KDE in panel (a). Panel (c): A simulated Gaussian resonance (peak) is added to the KDE with a specified intrinsic width (FWHM) and cross section as shown by the red line. The associated experimental width due to FAUST resolution is shown by the black line. The total background + peak distribution is sampled to the same level of counts as in panel (a).

with no resonant state yield is produced as shown in panel (b); this "background" distribution contains the same magnitude of statistical fluctuation as is present in the experimental distribution. Resonant states of varying intrinsic widths and cross sections (yields) can be added to the KDE to assess what state properties are necessary for confident identification among the fluctuations of the distribution. While the decay energy of a resonance follows a Breit-Wigner functional form, a Gaussian distribution serves as a good approximation [66]. The measured width of an excited state in FAUST is a convolution between the intrinsic width of the state and the resolution uncertainty in the excitation energy measurement as described by Equation 4.

$$\sigma_{measured} = \sqrt{\sigma^2_{intrinsic} + \sigma^2_{resolution}} \tag{4}$$

For any given excitation energy and intrinsic width, the measured width in FAUST can be calculated using the excitation energy dependent resolution previously calculated in Figure 1. A 138 MeV resonance with $\nu_{res.} = 2.0\%$ ($\sigma_{res.} = 108\,\mu b$) and intrinsic width (FWHM) of 3.1 MeV (giving a measured width of 4.0 MeV) is added to the KDE and sampled, providing a reasonable example of how the experimental distribution would appear if such a state were present as seen in panel (c). The total yield in the sampled background + peak distribution of panel (c) is kept consistent with the experimental 7-α yield (186097 counts).

Using this procedure, a simulated FAUST-measured 7-α excitation energy distribution using the state means and cross sections reported in the NIMROD experiment (Table 1) are shown for three intrinsic widths in Figure 12. A cross section of 30 µb is given to the 114 MeV state (similar to the reported cross section of the 138 MeV state), as no cross section was explicitly reported. The standardized residuals between the simulated spectra and the KDE background used in the sampling procedure are shown for each case. For this demonstration, the KDE background is assumed to have no associated uncertainty so that the standardized residuals represent the level of sensitivity to possible states given an exact background. For intrinsic widths up to 4 MeV FWHM, there are clear indications of resonant yield contributions in the simulated spectra and residuals. Given the ≈9.4 MeV FWHM 7-α excitation energy resolution of the NIMROD array, the widths and associated errors of the reported states indicate maximum intrinsic widths of ≈3.4 MeV and ≈2.6 MeV for the 126 MeV and 138 MeV states, respectively; the simulated spectrum in panel (b) is an approximate representation of the largest possible state width result consistent with the previous measurement. As an example of the difficulty in identifying resonant yield at the limit of large intrinsic width even with a perfect background description, panel (c) shows the result when this width is set to 9.0 MeV FWHM; while there is some indication of resonant yield in the residual plot of panel (f), identifying these states in practice is challenging due to imperfect background knowledge.

10.2. Statistical Likelihood Analysis for Cross Section Upper Limit

While the results of Figure 12 give an intuitive and qualitative indication that the state properties reported in ref. [18] would have produced rather obvious features in the 7-α excitation energy distribution of the present work, it is important to quantitatively assess the limits of toroidal state cross section, mean, and width where statistical significance can be claimed. One method for comparing the likelihood between two models for a given data sample is to compare the χ^2 between the fits. To this end, the procedure shown in Figure 11 can be used to create simulated spectra for each toroidal state mean over a broad range of cross sections and widths. Each simulated spectrum is then fit with the KDE background (including a free scaling parameter) and the KDE background (including a free scaling parameter) + a Gaussian peak (three free Gaussian parameters). The χ^2 of each fit is indicative of which model best describes the data. In both cases, there will be near perfect statistical agreement ($\chi^2/\nu = 1$) between the non-resonant portion of the spectrum and the fit. In reality, however, there is uncertainty associated with how well the background can be determined. If this uncertainty is not accounted for, such an analysis would provide an

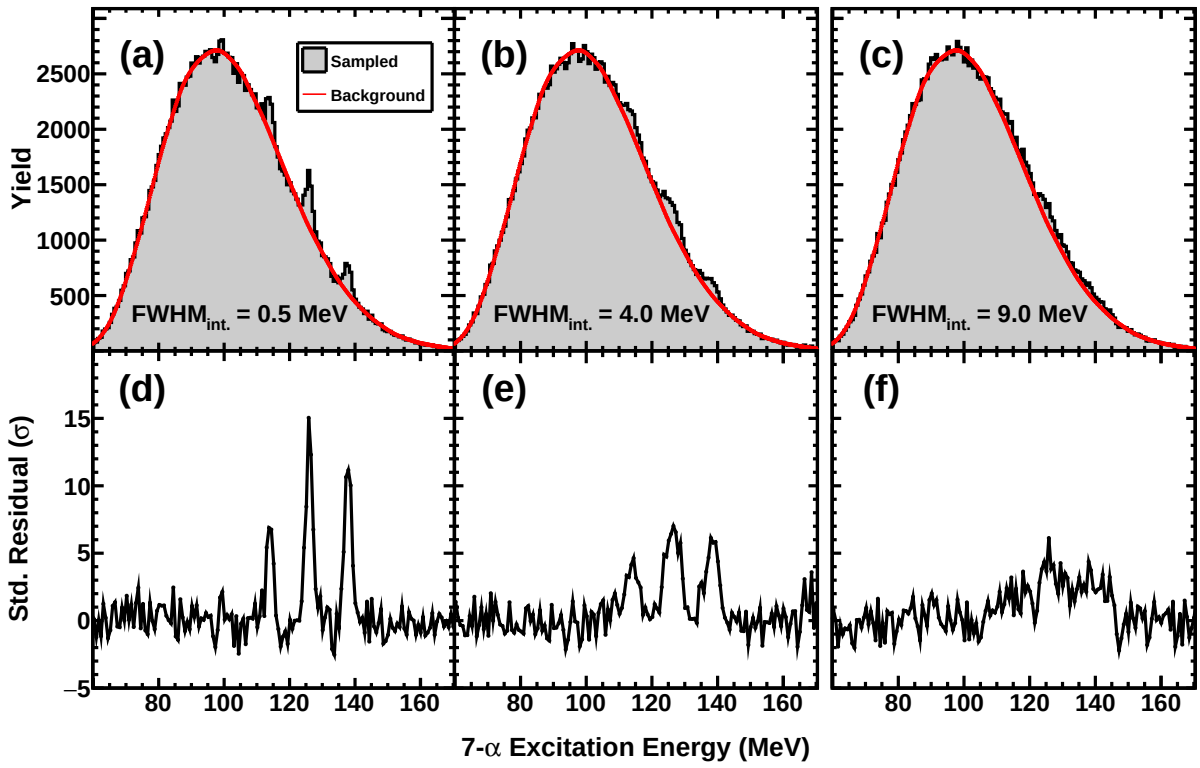

Figure 12: Simulated FAUST-measured 7-α distributions using the procedure of Figure 11 and the reported state cross sections and means of Table 1. A cross section of 30 µb is used for the 114 MeV state. Panels (a,b,c): Intrinsic state widths (FWHM) of 0.5 MeV (a), 4.0 MeV (b), and 9.0 MeV (c) are shown. Panels (d,e,f): Standardized residuals between the simulated spectra and the perfectly known background (KDE).

unfairly low estimate on the upper bounds of the cross section.

The details of the uncertainty in the background are difficult to constrain in practice. For the experimental data, inconsistencies in the shape of the produced background when using the event mixing technique for this data (Section 6.3) motivated the use of a polynomial background description. While the polynomial treatment should provide a background description capable of extracting resonant yield contributions with sufficiently narrow widths and high cross sections, this method becomes less applicable at the limits of broad widths and low cross sections as such states will drive the fit to describe them. One way to emulate these features of the background uncertainty is to add an associated error to the KDE background. For this purpose, the overall error was estimated to be the statistical uncertainly of the KDE model plus an additional approximated background uncertainty added in quadrature. The assumed background uncertainty was treated to scale with the statistical uncertainty, parameterized as $\sigma^2_{b.g.} = \beta\sigma^2_{stat.}$ so that:

$$\sigma_{Tot.} = \sqrt{\sigma^2_{stat.} + \beta\sigma^2_{stat.}} \tag{5}$$

where $\sigma_{Tot.}$ is the total background error, $\sigma_{stat.}$ is the statistical error associated with the KDE ($\sqrt{yield}$), and β is a scaling factor to account for the general uncertainty in the back-

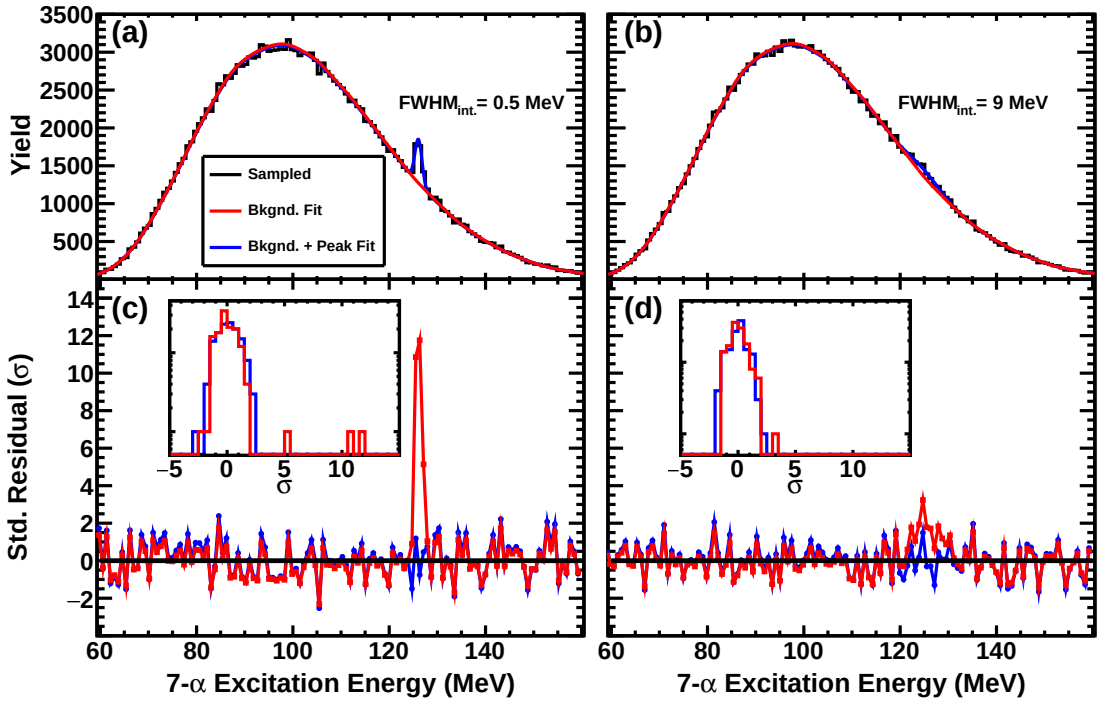

Figure 13: Statistical likelihood analysis procedure. Panels (a,b): Simulated FAUST-measured 7-α distributions (black) containing resonant yield peak with intrinsic FWHM of 0.5 MeV (a) and 9.0 MeV (b) using the procedure of Figure 11 and fit using the background model (red) and peak model (blue) (as described in the text). Panels (c,d): Standardized residuals obtained from the background model and peak model. Insets show the projection of the standardized residuals for the two models; the uncertainty associated with the background model causes the distribution to generally be narrower than the peak model distribution.

ground. The magnitude of this error when using $\beta = 0.5$ is shown by the shaded region in panel (a) of Figure 11. In simple terms, this error region allows for the "true" background to be any distribution reasonably contained within these limits, in effect allowing for a shape uncertainty in the background. The fitting procedure previously described is performed on simulated resonance spectra as shown in Figure 13 where the KDE background fit (background model - red curve) possesses this error and the KDE background + peak fit (peak model - blue curve) does not. The standardized residuals in panel (c) give a graphical indication of the goodness of each fit. For the background model, the increased error over the peak model emerges as a slight compression of the residuals centered about $\sigma = 0$, giving a reduction in the χ^2 for the non-resonant portions of the spectrum; however, the background model does not fit the resonant yield contribution, giving increased χ^2 over the peak model in this region. The standardized residual projection of each fit is given in the inset showing the slightly narrower distribution for the background model over the peak model for the bulk of the data but possessing a few extreme outliers associated with the peak region. The model that best describes the sampled spectrum is chosen as the one with the smaller χ^2 (for panel

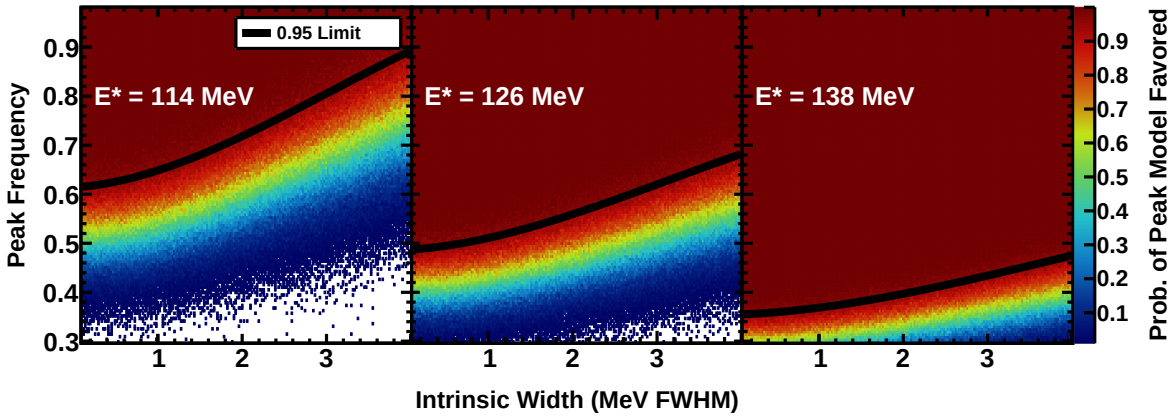

Figure 14: Statistical likelihood analysis results between the background and peak model for resonant states simulated at 114 MeV (a), 126 MeV (b), and 138 MeV (c). The probability that the peak model is preferred over the background model (p_p) is shown as a function of the intrinsic width (MeV FWHM) and relative frequency (resonant yield to total yield). A 3$^{\text{rd}}$ order polynomial is fit to the $p_p = 0.95$ boundary as shown by the black curves.

(a,c) the peak model is preferred). Panel (b) shows this same procedure for a simulated spectrum for a peak with the same cross section as panel (a) but a much broader width. The slightly compressed residuals for the background model compensate for any enhancement associated with the peak, resulting in preference of the background model for this case.

This simulated spectra fitting procedure is performed as a function of the intrinsic width and relative frequency (ratio of resonance yield to total sampled yield) for the three reported state means as shown in Figure 14. For each pixel in these plots, the distribution sampling and fitting procedure is independently performed 200 times to aptly account for the broad range of statistical fluctuations that can occur during sampling. The color scale corresponds to the ratio of times the peak model fit has a lower χ^2 than the background model, indicating that it is a better description of the data. The boundary where this ratio is equal to 0.95 is shown by the 3$^{\text{rd}}$ order polynomial in each panel. For a given relative frequency (and by extension, cross section) there is greater sensitivity in regions with less background due to the larger signal to background ratio. The background yield from panels (a) to (c) is decreasing, reducing the required resonance yield for peak model preference. The relative frequency axis can be transformed to cross section using the AMD + GEMINI++ procedure previously described; while there will be large systematic uncertainties in the absolute cross section estimate, the replicated procedure allows for comparison to previous work, as the primary difference between the two experiments is detection efficiency. Figure 15 shows the upper limit for statistical significance of the three NIMROD-reported state means as a function of the intrinsic width and cross section. The dashed horizontal lines indicate the allowable intrinsic widths of the states measured in NIMROD according to the detector resolution and measured widths. Based on the data acquired from experiment and calculations performed in this section, an approximate but fair comparative upper limit to ref. [18] for toroidal high-spin isomer cross section in this reaction channel is obtained. For the two states that

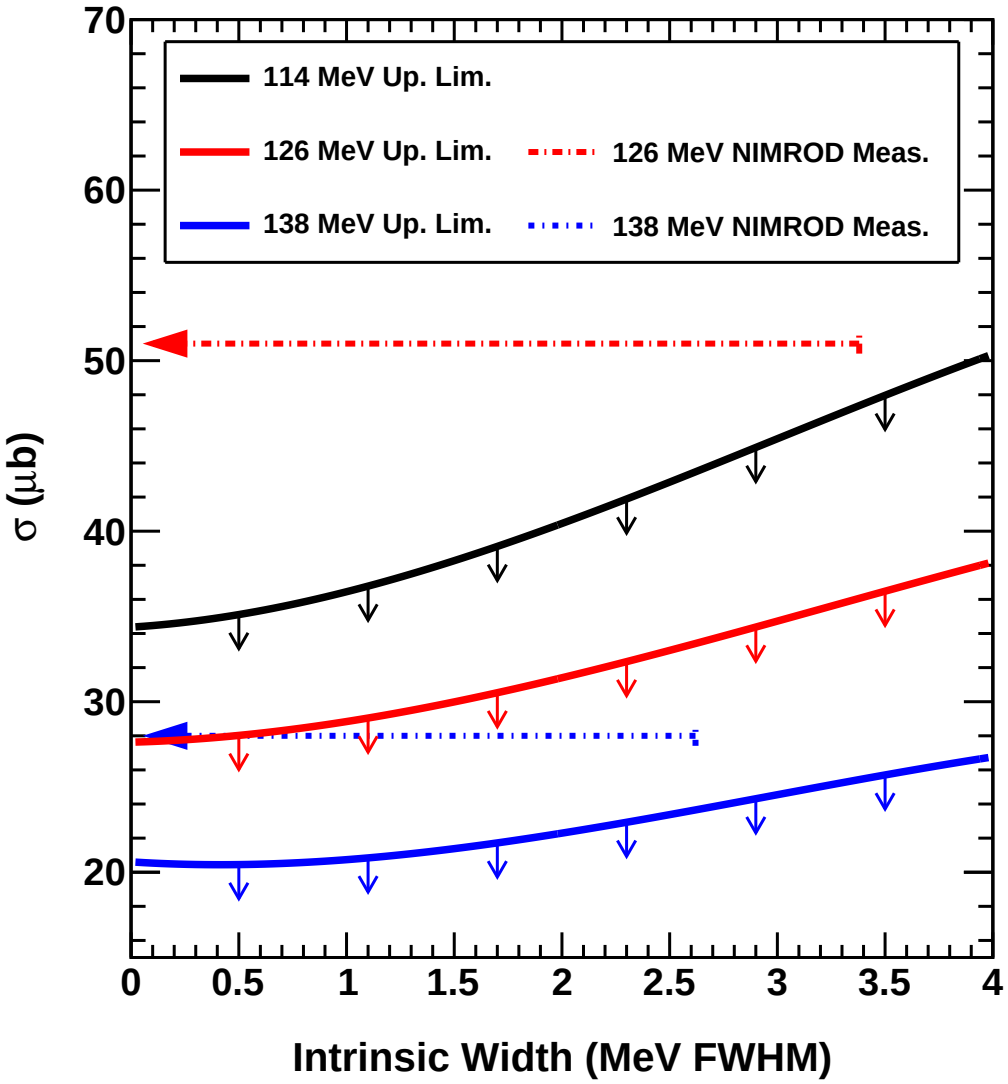

Figure 15: Comparison between the FAUST upper limit of toroidal high-spin isomer cross section (solid lines) using a background uncertainty parameter of $\beta = 0.5$ to the cross sections reported in ref. [18] (dashed horizontal arrows). Arrows indicate the range of allowable intrinsic widths of reported states consistent with the experimental resolution.

had reported cross sections (126 MeV and 138 MeV), the obtained upper limits fall well below what was reported.

Accurately determining the magnitude and characteristics of the background uncertainty free of bias is a challenging and considerable undertaking. It is important to note that the estimated background error for this analysis is an ansatz and is included to approximate the level of uncertainty that may exist. The selection of the error parameter ($\beta = 0.5$) was guided by inspecting simulated spectra determined to be significant and ensuring that these spectra contained qualitatively distinguishable features. Effort was placed to ensure that

the uncertainty approximation was generous to give a conservative cross section upper limit. Further, the features seen in the FAUST-simulated spectra using the broadest allowable intrinsic width consistent with previous measurement (panel (b) of Figure 12) indicate that such resonances would be readily seen in the present data if they possessed the properties that were suggested.

11. Conclusion

Theoretical predictions suggest that angular momentum stabilized toroidal high-spin isomers of intermediate mass α-conjugate nuclei may exist. A prior experiment observed possible evidence of toroidal α-disassembling ^{28}Si states, but due to limited angular resolution and moderate statistical uncertainties, a confirmation experiment was necessitated. The current experiment was designed to confidently and accurately measure such states if their widths and cross sections were on the order suggested by the prior experiment. To this end, collision data of ^{28}Si + ^{12}C at 35 MeV/nucleon was recorded using position-sensitive FAUST, giving over an order of magnitude increase in the number of measured collisions over the previous experiment. Improvements to the pulse-processing technique and data acquisition allowed for significantly higher event rates and a reduction in position-dependent distortions over past FAUST experiments. Despite the optimized experimental conditions for measuring the proposed states, no strong evidence was found for statistically significant resonant state yield in the seven α-particle channel. Given the significant amount of collected collision data and high multiplicity efficiency of FAUST, examination of the eight α-particle channel was permitted to search for similar predicted states in ^{32}S; however, a similar lack of resonant state evidence was found. Upon closer inspection of the collision properties of measured 7,8-α events, it was revealed that the observed breakup properties are consistent with a significant fraction of such breakups not originating from clean, excited ^{28}Si* or ^{32}S* breakups. A detailed statistical significance analysis revealed that the sensitivity of the current measurement confidently excludes the reported state properties claimed in the previous experiment; however, it does not exclude the possible presence of exotic breakup configurations, including toroidal states, that may lead to such channels. There may be yield associated with toroidal high-spin isomer breakup in the presented spectra, but the sensitivity of the current measurement is incapable of claiming statistical significance of any observed features.

12. Acknowledgements

Supported by the following: Department of Energy Grant DE-FG02-93ER40773 & Welch Foundation Grant A-1266. We would like to thank the staff of the Cyclotron Institute for providing excellent beams.

References

[1] H. Schuler and T. Schmidt., Deviations of the atomic nucleus from spherical symmetry, Z. Physik 94 (1935) 457.

[2] A. Bohr, Nuclear magnetic moments and atomic hyperfine structure, Phys. Rev. 81 (1951) 331.

[3] A. Bohr and B. Mottelson, Nuclear magnetic moments and atomic hyperfine structure, Phys. Rev. 89 (1953) 316.

[4] J. Rainwater, Nuclear energy level argument for a spheroidal nuclear model, Phys. Rev. 79 (1950) 432.

[5] J. Griffin and J.A. Wheeler, Collective motions in nuclei by the method of generator coordinates, Phys. Rev. 108 (1957) 311.

[6] S.G. Nilsson, Binding states of individual nucleons in strongly deformed nuclei, Ph.D. thesis, Inst. Theor. Phys., Univ. Copenhagen, 1955.

[7] J.A. Wheeler, Nucleonics notebook, (unpublished) (1950). See also p. 297 in G. Gamow, Biography of Physics, Harper & Brothers Publishers, N. Y. 1961; Princeton University Graduate Course Physics 576 Take-Home Examination Problem 2, May 22, 1963 (unpublished).

[8] C.Y. Wong, Toroidal nuclei, Phys. Lett. B 41 (1972) 446.

[9] C.Y. Wong, Toroidal and spherical bubble nuclei, Ann. Phys. 77 (1973) 279.

[10] C.Y. Wong, Rotating toroidal nuclei, Phys. Rev. C 17 (1978) 331.

[11] T. Ichikawa et al., Pure collective precession motion of a high-spin torus isomer, Phys. Rev. C 89 (2014) 011305.

[12] T. Ichikawa, J.A. Maruhn, N. Itagaki, K. Matsuyanagi, P.-G. Reinhard, and S. Ohkubo, Existence of an exotic torus configuration in high-spin excited states of ^{40}Ca, Phys. Rev. Lett. 109 (2012) 232503.

[13] P. Ring, P. Schuck, The Nuclear Many-Body Problem, Theoretical and Mathematical Physics, Springer Berlin, Heidelberg, 1981, p. 142.

[14] A. Staszczak and C.Y. Wong, A region of high-spin toroidal isomers, Phys. Lett. B 738 (2014) 401.

[15] A. Staszczak and C.Y. Wong, Toroidal high-spin isomers in light nuclei with N≠Z, Phys. Scr. 90 (2015) 114006.

[16] X.G. Cao et al., Evidence for resonances in the 7α disassembly of ^{28}Si, AIP Conference Proceedings 2018 (2018) 020021.

[17] Z.X. Ren, P.W. Zhao, S.Q. Zhang, and J. Meng, Toroidal states in ^{28}Si with covariant density functional theory in 3D lattice space, Nuc. Phys. A 996 (2020) 121696.

[18] X.G. Cao, E.J. Kim, K. Schmidt, K. Hagel, M. Barbui, J. Gauthier, S. Wuenschel, G. Giuliani, M.R.D. Rodriguez, S. Kowalski, H. Zheng, M. Huang, A. Bonasera, R. Wada, N. Blando, G.Q. Zhang, C.Y. Wong, A. Staszczak, Z.X. Ren, and J.B. Natowitz, Examination of evidence for resonances at high excitation energy in the 7α disassembly of ^{28}Si, Phys. Rev. C 99 (2019) 014606.

[19] A. Bohr, B. Mottelson, Nuclear Structure, volume 2, Benjamin, New York, 1975.

[20] A. Gaamouci et al., Exotic toroidal and superdeformed configurations in light atomic nuclei: Predictions using a mean-field Hamiltonian without parametric correlations, Phys. Rev. C 103 (2012) 054311.

[21] H. Zheng and A. Bonasera, Spin quantization in heavy ion collision, Symmetry 13 (2021) 1777.

[22] G. Gamow, Mass defect curve and nuclear constitution, Proc. Math. Phys. Eng. 126 (1930) 632–644.

[23] E. Pairam and A. Fernandez-Nieves, Generation and stability of toroidal droplets in a viscous liquid, Phys. Rev. Lett. 102 (2009) 234501.

[24] J.D. McGraw et al., Plateau-rayleigh instability in a torus: formation and breakup of a polymer ring, Soft Matter 6 (2009) 1258–1262.

[25] M.A. Fontelos, V.J. García-Garrido, and U. Kindelán, Evolution and breakup of viscous rotating drops, SIAM Journal on Applied Mathematics 71 (2011) 1941–1964.

[26] S.E. Agbemava and A.V. Afanasjev, Hyperheavy spherical and toroidal nuclei: The role of shell structure, Phys. Rev. C 103 (2021) 034323.

[27] S. Wuenschel et al., NIMROD-ISiS, a versatile tool for studying the isotopic degree of freedom in heavy ion collisions, Nucl. Instr. and Meth. A 604 (2009) 578–583.

[28] W.W. Wilcke et al., Reaction parameters for heavy-ion collisions, At. Data Nucl. Data Tables 25 (1980) 389–619.

[29] M. Aslin, A. Hannaman et al., A new waveform analysis technique to extract good energy and position resolution from a dual-axis duo-lateral position-sensitive detector, Nucl. Instr. and Meth. A 985 (2021) 164674.

[30] A. Hannaman et al., High event rate analysis technique for the dual-axis duo-lateral position-sensitive silicon detectors of FAUST, Nucl. Instr. and Meth. A 1050 (2023) 168130.

[31] E.K. Warburton, R-matrix analysis of the $\beta^{\mp}$-delayed alpha spectra from the decay of ^{8}Li and ^{8}B, Phys. Rev. C 33 (1986) 303.

[32] D. Jenkins and O. Kirsebom, The secret of life, Physics World 26 (2013) 23.

[33] J.H. Kelley, J.E. Purcell, and C.G. Sheu, Energy levels of light nuclei A = 12, Nucl. Phys. A 968 (2017) 71–253.

[34] M.B. Tsang et al., Comparisons of statistical multifragmentation and evaporation models for heavy-ion collisions, Eur. Phys. J. A 30 (2006) 129–139.

[35] K. Hagel et al., Violent collisions and multifragment final states in the ^{40}Ca+^{40}Ca reaction at 35 MeV/nucleon, Phys. Rev. C 50 (1994) 2017.

[36] A. Hannaman et al., Isoscaling and nuclear reaction dynamics, Phys. Rev. C 101 (2020) 034605.

[37] Y. Larochelle et al., Dependence of intermediate mass fragment production on the reaction mechanism in light heavy-ion collisions at intermediate energy, Phys. Rev. C 53 (1996) 823.

[38] J. Pochodzalla et al., Two-particle correlations at small relative momenta for ^{40}Ar-induced reactions on ^{197}Au at E/A=60 MeV, Phys. Rev. C 35 (1986) 1695.

[39] A.M. Lane and R.G. Thomas, R-matrix theory of nuclear reactions, Phys. Mod. Phys. 30 (1958) 257.

[40] A.B. McIntosh et al., Tidal effects and the proximity decay of nuclei, Phys. Rev. Lett. 99 (2007) 132701.

[41] G. Verde, A. Chibihi, R. Ghetti, and J. Helgesson, Correlations and characterization of emitting sources, Eur. Phys. J. 30 (2006) 81–108.

[42] D. Drijard, H.G. Fischer, and T. Nakada, Study of event mixing and its application to the extraction of resonance signals, Proceedings 225 (1984) 367–377.

[43] M Barbui et al., Searching for states analogous to the ^{12}C Hoyle state in heavier nuclei using the thick target inverse kinematics technique, Phys. Rev. C. 98 (2018) 044601.

[44] A. F. Nassirpour, Improved event mixing for resonance yield extraction, Proceedings 10 (2019) 26.

[45] A. Ono et al., Antisymmetrized version of molecular dynamics with two nucleon collisions and its application to heavy ion reactions, Prog. Theor. Phys 87 (1992) 1185–1206.

[46] A. Ono and H. Horiushi, Antisymmetrized molecular dynamics for heavy ion collisions, Prog. Part. Nucl. Phys. 53 (2004) 501–581.

[47] R. Wada et al., Entrance channel dynamics in ^{40}Ca + ^{40}Ca at 35A MeV, Phys. Lett. B 422 (1998) 6–12.

[48] R. Wada et al., Reaction dynamics and multifragmentation in fermi energy heavy ion reactions, Phys. Rev. C 69 (2004) 044610.

[49] R. Charity, GEMINI: A code to simulate the decay of a compound nucleus by a series of binary decays, Joint ICTP-IAEA advanced workshop on model codes for spallation reactions (2008) 139–148.

[50] K.W. Brown et al., Proton-decaying states in light nuclei and the first observation of ^{17}Na, Phys. Rev. C 95 (2017) 044326.

[51] R.J. Charity et al., Invariant-mass spectroscopy of ^{18}Ne, ^{16}O, and ^{10}C excited states formed in neutron-transfer reactions, Phys. Rev. C 99 (2019) 044304.

[52] C.B. Das et al., Statistical simultaneous multifragmentation model for heavy ion collisions with entrance channel characteristics, Phys. Rev. C 53 (1996) 1833.

[53] V.E. Voila et al., Light-ion-induced multifragmentation: The ISiS project, Phys. Rep. 434 (2006) 1–46.

[54] H.-Y. Wu et al., Evolution of the decay of highly excited nuclei, Phys. Rev. C 57 (1998) 3178.

[55] B. Borderie et al., Temperature and density conditions for alpha clustering in excited self-conjugate nuclei, Symmetry 13 (2021) 1562.

[56] M. Bruno et al., Simple observables sensitive to the transition from sequential decay to simultaneous break-up of nuclear systems, Nuov Cim A 105 (1992) 1629–1635.

[57] J. Bishop et al., Experimental investigation of α condensation in light nuclei, Phys. Rev. C 100 (2019) 034320.

[58] J. Manfredi et al., α decay of the excited states in ^{12}C at 7.65 and 9.64 MeV, Phys. Rev. C. 85 (2012) 037603.

[59] B.K. Nandi et al., Search for DCC in relativistic heavy-ion collision through event shape analysis, Phys. Lett. B 449 (1999) 109–113.

[60] D.A. Cebra et al., Event-shape analysis: sequential versus simultaneous multifragment emission, Phys. Rev. Lett. 64 (1990) 2246.

[61] A. Badala et al., ^{16}O breakup on Al, Ni and Au targets at 95 MeV/nucleon, Phys. Lett. B 299 (1993) 11–15.

[62] L. Beaulieu et al., Breakup of highly excited ^{35}Cl projectiles on a gold target at 30 A MeV: an exclusive analysis, Phys. Rev. C 580 (1994) 81–99.

[63] K. Schmidt et al., Alpha conjugate neck structures in the collisions of 35 MeV/nucleon ^{40}Ca with ^{40}Ca, Phys. Rev. C 95 (2017) 054618.

[64] C.P. Montoya et al., Fragmentation of necklike structures, Phys. Rev. Lett. 73 (1994) 3070.

[65] M. Rosenblatt, Remarks on some nonparametric estimates of a density function, Ann. Math. Statist. 27 (1956) 832–837.

[66] P.A.M. Dirac, The quantum theory of the emission and absorption of radiation, Proc. R. Soc. A 114 (1927) 243–265.